A study of normal fault structure and along-strike variations, based on the northern Moab fault system, Utah

Master Thesis Earth Science

Lucas Corrêa Tonon D'Almeida

Department of Earth Science

University of Bergen

November 2022

Abstract

Fault systems are complex structures where multiple elements generate a network that can deeply impact fluid flow, affecting subsurface hydrocarbon and groundwater reservoirs. However, seismic data from such structures are hampered by data resolution, while field mapping, where much more details are seen, faces the challenge of outcrop quality and abundance. In this work, I combined these two data sources, a series of canyons that cut through a fault splay belonging to the Moab Fault system in southern Utah, USA, and large-scale fault systems found in the North Sea rift, to evaluate how seismic data resolution can influence our perception of fault complexity. As many variables control how fault systems are imaged in seismic surveys, it is important to understand how different parameters impact structural imaging to avoid pitfalls. By generating models based on the Utah outcrops, it was possible to produce seismic equivalents and then use a 2D Point Spread Function-based convolution method of modelling to assess how the models would be seismically imaged. As seismic imagery is also affected by many parameters like Dominant frequency, Angle of illumination, Critical angle and Noise, during the modelling, these were modified to different values to verify their impact in the imaging of fault structures.

The images generated in this study demonstrate how challenging it can be to properly image and interpret small displacement faults and associated structures. The detectability of normal faults and their structures depends mostly on the size of the displacement and the reflectivity between the units juxtaposed by the fault. Concerning seismic parameters affecting fault visibility, the dominant frequency and illumination are two of the most important. The first allows for the observation of smaller structures the higher it becomes. The second parameter points to whether a surface will be illuminated in the seismic. However, the illumination parameter may be of little use in real normal fault seismic images, as most structures have a dip angle higher than the maximum illumination angle found in seismic surveys. Other parameters, like the incident angle and noise, tend to reduce the visibility of structures in fault zones, so they should always be as low as possible. In comparing the synthetic seismic produced here with the real one, it was noticed that many low displacement faults could appear as small "bumps" or anticlines that could be mistaken by drag structures. This problem can sometimes be solved by moving the image along strike as the change in the displacement may become enough to make the fault visible.

Acknowledgements

On the final days of these two long years in the MSc program in the Geodynamics and Basin Studies at the Department of Earth Sciences at the University of Bergen, I need to first and foremost express my gratitude to my three supervisors that made this herculean effort of helping me getting an MSc degree. Haakon Fossen is thanked for his most valuable guidance and support during this time. Isabelle Lecomte is thanked for all the feedback and all the support in learning some of the trickiest software I had to use during all my studies. And Casey Nixon is also thanked for all his feedback and great ideas used to build this thesis. I also would like to thank Lucas Valore and Casper Flæte not only for their many bits of help in gathering some data and with some softwares but for being able to withstand my inability to keep my mouth shut, which caused me to talk about everything all the time. A special thanks are also needed to Leo Zijerveld for setting up the remote desktop access and for helping me more than once, even with the simplest of questions.

For granting access to crucial softwares that made this thesis possible, I also thanks Schlumberger (Petrel), Norsar (SeisRoX), MathWorks (Mat-Lab), Adobe (Adobe Illustrator) and VOG (LIME). Other thanks go to CGG for the access agreement allowing access to the DISKOS database and seismic data.

All the fantastic and supportive people I have met during my stay in Bergen also have all my gratitude for helping my mind stay afloat. A special thanks to Lucas Valore and Flávio Almeida for the many amazing days and time spent here. Many thanks are also due to all the PhD gang and MSc students I had the pleasure to meet during my lectures or lunch breaks. And not only in Bergen, but many of my thanks also go to my friends back home that made many of my lonely nights fun and bearable, with special thanks to my friends: Mariana, Geovana and Fernanda.

At last, I would like to send my thanks and all my love to my family back home, that supported me here in all ways possible and will always be one of the most important part of my life.

v

Contents

List of Figures

List of Tables

Nomenclature

D - Dune

ID - Interdune

Fm - Formation

FW – Full Wavefield

I$_{SR}$ – Illumination Vector

Mb - Member

Mdst - Mudstone

PSDM – Prestack Depth Migrated

PSF – Point Spread Function

R – Receiver

RB – Ray Base

S – Shot

Sdst - Sandstone

VE – Vertical Exaggeration

VO – Virtual Outcrop

Vp – Compressional Wave velocity

Vs – Shear Wave Velocity

1.Introduction

1.1 Motivation

Fault systems and their complications have been the target of many studies in the past, particularly regarding extensional faults (Peacock et al., 1994; Childs et al., 1996; Knott et al., 1996; Shipton and Cowie, 2001; Davatzes et al., 2003; Johansen and Fossen, 2008; Schueller et al., 2013). A well know example of such a normal fault system is of the Moab Fault system in southern Utah, US, near the Arches National Park, cutting rocks of the Paradox Basin and overlaying Mesozoic layers with a throw of up to 1 km (Davatzes and Aydin, 2005; Johansen and Fossen, 2005). These types of faults and the network formed by them are a point of interest for many different industries, such as mining, oil, water and CO_2 storage, due to how they can serve as conduits or barriers to fluid flow in the rocks (Caine et al., 1996; Zhang and Sanderson, 1996; Sanderson and Zhang, 1999; Berg and Skar, 2005; Fossen et al., 2005; Fossen and Rotevatn, 2016).

Faults, with all their associated complexities, form a complex network of interacting structures of an extensive range of scales. These interactions often create local stress perturbations that increase the extent of the damage zone and the frequency of new structures such as deformation bands, joints and new small faults (Kim et al., 2004; Nixon et al., 2014; Fossen and Rotevatn, 2016). This creates a challenge when faults are mapped from seismic data because many of these structures are below seismic resolution. However, even faults with low displacement may impact subsurface flow through changes in rock permeability, baffling or perturbing the flow pattern in a reservoir production or injection situation (Loveless et al., 2011). Although identifying these small structures in seismic imagery is difficult or impossible, they are easily observed in surface outcrops, which can then be used as analogues or models for subsurface cases (e.g., Rotevatn et al., 2007).

To explore to what extent fault complexities are imaged in seismic data, synthetic seismic can be applied. Seismic resolution depends on the wave velocity and frequency, giving us a value on the minimum resolution in the image. Illumination is another important factor, as its affects the lateral resolution. Acoustic impedance, layers thickness and size of structures, can all be implemented and varied in synthetic models. To properly validate geological models constructed based on seismic data, seismic modelling is critical to constrain the level of uncertainty represented by a given seismic survey (Lecomte et al., 2015). The exposed outcrops in Utah serve as an excellent analogue for small subseismic-scale structures that probably are

representative of faults in most other regions dominated by normal faulting, such as the North Sea rift. Using those outcrops and their structures to produce synthetic seismic images will, therefore, expand our knowledge on seismic images and potential limits and pitfalls of seismic imaging complex geological structures.

1.2 Aims and Objectives

This thesis aims to further our understanding of the complexities of faults and fault zones and to what extent such complexities are captured in seismic data, based on synthetic modelling of real field examples. To achieve this objective, the following steps were taken:

1. To define a workflow for building a geological model of fault zones and their complexities.

2. To produce high-resolution geometrical models of exceptionally exposed fault outcrops in Utah by using high-resolution virtual models in LIME and outcrops observations during fieldwork.

3. To generate 2D synthetic seismic, based on Utah outcrops.

4. To analyze the effect of various geophysical parameters to understand how they affect the seismic imaging of differently sized structures.

5. To compare the synthetic seismic results with real seismic examples.

1.3 Approach

To explore the imaging of small-scale structural features in seismic data, surface outcrop analogues of normal faults arrays from Utah, US, were mapped and used to construct 2D and 3D geological models. The 2D models were then used to generate synthetic seismic images using a Point-Spread Function (PSF) convolution method. The models and images generated were then compared to seismic data from the North Sea near Norway, both in its real-size and upscaled version, to look for and compare similar structures and to describe how smaller ones may behave or appear under seismic images.

1.4 Thesis Outline

This thesis is structured as follows:

Chapter 1: Introduction to the thesis topic, the objective and goals, and a short paragraph about the approach taken.

Chapter 2: General background on normal faults and their damage zones and anatomy, and an overview of current terminology.

Chapter 3: Geological setting for both the Paradox Basin and the structures found near the Moab Fault and the general setting for the geology of the northern North Sea.

Chapter 4: Theoretical basis for seismic modelling and virtual outcrop software.

Chapter 5: Methodology used in this study, and the workflow used to interpret the virtual outcrops and the steps and parameters used to generate the synthetic seismic models.

Chapter 6: Results obtained through the synthetic seismic modelling and comparison with real seismic data.

Chapter 7: Discussion of results.

Chapter 8: Conclusion and suggestions for future work.

2.Theoretical Background

2.1 Fault anatomy

While faults are usually interpreted as surfaces on seismic data, more detailed field-based studies of faults reveal that they are not just a simple "discrete" plane or surfaces, but irregular volumes of deformed rock are composed of many different elements beyond the slip surface (e.g., Braathen et al., 2009). The volume that contains all these structures is commonly referred to as the Fault Zone (Figure 2.1). Internally, a fault zone is structurally and petrophysical heterogeneous, with specific trends and zonation that may be complex, although with a general increase in structural complexity towards its central part. A very generalized model sub-divides fault zones into two distinct structural and hydrogeological units: A central *fault core* and an enveloping *damage zone* (Caine et al., 1996).
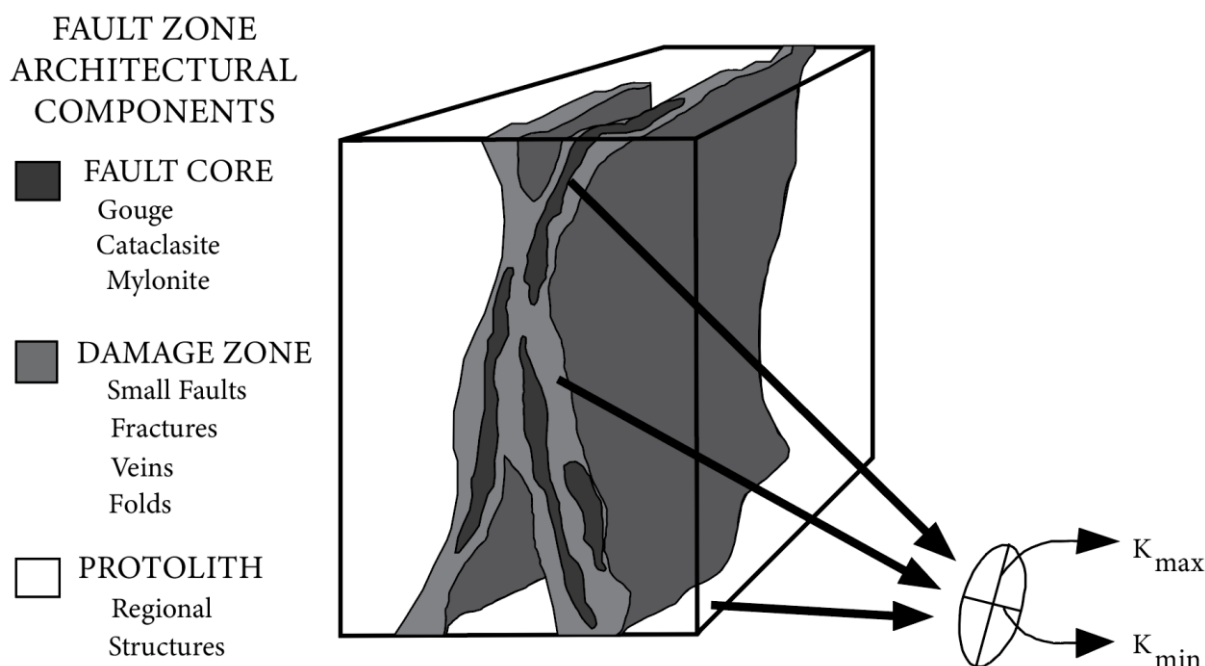
Figure 2.1: A conceptual model of fault zone with accompanied architectural components. Modified from Caine et al. (1996).

2.2.1 Fault core

Forming the central part of the fault, the fault core is a high-strain zone where most displacement has accumulated (~95%), encompassing the main slip surface and, depending on the lithology, a zone of strongly sheared rocks (Caine et al., 1996; Fossen et al., 2020). Poorly lithified rocks and shale will have clay-rich gouge zones, shale smears, and deformation band

shear zones (Davatzes & Aydin, 2005; Loveless et al., 2011), while strong lithified rocks are more likely to have cataclasites, breccias or geochemically altered zones, although clay-rich fault gouge can develop in any host rock setting (Caine et al., 1996; Fossen et al., 2020). To add to the complexity of the Fault Core, less deformed lenses of host rock can be incorporated into it, which defines the core as an anastomosing network rather than just a single zone.

Due to shear-induced grain-size reduction and precipitation of minerals, the permeability and porosity of the fault core can be drastically changed compared to the damage zone and the protolith, leading the fault core to function as and barrier for fluid flow frequently (Caine et al., 1996; Fossen, 2020).

2.2.2 Damage Zone

A damage zone is a volume of deformed rock surrounding the fault core and possesses relatively low-displacement structures (Knott, 1996; Kim & Peacock, 2004). While the damage zone is generated prior to the development of the main fault slip surface or gouge zone, it may expand as new structures like shear fractures, veins, shorth joints, deformation bands, and stylolites are formed (Fossen, 2020). The extent of the damage zone is estimated based on the distribution of fracture frequency per unit interval across a fault until the number of fractures or chosen structure is reduced to the same frequency as the background one (Gudmundsson et al., 2010; Schueller et al., 2013; Choi et al., 2016). Smaller faults in the damage zone may have their own damage zones, increasing the overall damage zone width (Shipton & Cowie, 2001. Fossen, 2020). As the stress is mainly concentrated on the inner parts of the zone, the density of structures is higher there compared to the outer regions, where the number of deformation structures gradually decay away from the fault core, as can be seen in the case of deformation bands in sandstones, where the decrease can be described as logarithmic (Schueller et al., 2013; Choi et al. 2016). The width of the damage zone is also impacted by variations in the lithology, fault geometry and growth/linkage history (Childs et al., 1996; Kim & Peacock, 2004; Johansen & Fossen, 2008).

The damage zone generally involves changes in permeability in ways that depend on the type of structure formed. The permeability change associated with the damage zone structures can be negative (reduction, e.g., deformation bands) or positive (increase, e.g., joints and fractures), and fault zones may therefore serve as both baffles and conduits for fluid flow. Because these zones show a variety of geometries and fault patterns, Kim et al. (2004) divided them into three different main zones based on their positions along the fault: Tip damage zones, Linking damage zones and Wall damage zones.

2.3 Fault Growth

Faults grow from small fractures that propagate laterally, interact and link up to form longer structures. They can form spontaneously but can also evolve from pre-existing structures such as joints and dike margins (Childs et al., 1995, Walsh et al., 2002, Walsh et al., 2003, Fossen et al., 2020). Fault growth has been divided into two distinct end-member models: The isolated fault model and the Coherent fault model (Childs et al., 1995). In the Isolated fault model, the displacement accumulates progressively as the fault length increases through lateral propagation, where overlapping is incidental to previously unrelated faults (Cartwright et al., 1995; Childs et al., 1995). Although this first model is based on a scenario where no pre-existing structures are present, most cases involve the existence of previous structures, influencing the fault growth. This is the key element of the Coherent fault model, where fault lengths are quickly established and kept near-constant from an early stage, while the displacement accumulates as long as the fault is still active. Hence, fault growth is dominated by displacement accumulation without lengthening until the fault displacement to length ratio reaches a point where the differential stress is high enough to drive tip propagation (Peacock & Sanderson 1991; Cartwright et al. 1995; Walsh et al. 2002; Walsh et al. 2003)

Most normal faults have a displacement gradient of around 0.1-0.01 throughout their length (Fossen et al., 2020). However, the displacement accumulation can vary along the fault due to lithologic variations, conjugate fault interactions, fault bends and, in particular, fault linkage (Peacock, 1991).

2.4 Fault Linkage

As faults grow and expand, they will interact and link up with other faults to form much longer faults. This process of fault linkage is the most common and efficient way for faults to grow in length, forming overlap zones of two or more fault strands and an anomalously wide damage zone. The linkage process between two subparallel faults starts when the two fault tips get close enough to cause an interaction between their zones of stress perturbation and elastic strain field that is large enough to influence their propagation paths (Fossen et al., 2020). The overlap of these two regions is known as the overlap or relay zone and is characterised by a rapid loss in displacement on the two overlapping faults. A relay ramp is then created between the overlapping fault tips. A ramp is a region where layers are bent, defining a relatively complex

volume of small-scale deformation structures and anomalously oriented minor faults. The distributed displacement and anomalously wide and well-developed damage zone make relay zones locations of anomalous fluid flow that often improve reservoir communication (Fossen & Rotevatn, 2016).

Non-parallel faults can also link up from longer structures. This often generates abutting faults, where one fault tip propagates into another fault, creating an intersection line or point (Peacock et al., 2016). As the abutting faults start to interact, there is a temporary shift of nearly 90° of the extension direction, returning to normal as soon as the spots become geometrically hard-linked (Gent & Urai, 2020) and form a coherent three-block system and a Y-type fault interaction (Peacock et al., 2017).

Linkage of faults and fractures occurs at almost any scale, from the linkage of microcracks via mesoscopic shear fractures to the linking of large faults segments

2.5 Fracture network

A fracture network is formed when fractures interact to create an interlinked system (Peacock, 2016). These networks display a large range of sizes, lengths, orientations, and scales, usually defined by local characteristics like intensity and direction of stress and lithology (Soliva et al., 2006). Secondary faults can develop due to the disturbance of the regional stress field created by already formed larger faults. The new faults have their location and orientation controlled by these stress disturbances. These new and smaller faults may have orientations and properties different from their earlier nearby larger faults (Maerten et al., 2002). This causes the behaviour of smaller faults to be possible to predict by downscaling the larger ones in case of subseismic faults (Bailey et al., 2002).

The formation of these networks and the knowledge about their complexities are of great value as they can enhance the connectivity between the fractures and faults, impacting the fluid flow and the formation of oil, gas or ore deposits (Fossen & Rotevatn, 2016). Along with increased connectivity of faults, there is also increased compartmentalization of porous reservoirs, communication in nonporous reservoirs, and changes in the pattern of reservoir juxtaposition.

2.6 Drag

The drag zone is considered a zone of fault-related folding, showing up as deflections of curved markers adjacent to a fault (Kearey, 1993; Grasemann et al., 2005). Even though these ductile

structures are found adjacent to faults and contribute to the total displacement, they are not part of the fault per se. Their length can vary immensely, ranging from less than a meter to several kilometers, and varying vertically when layers of different mechanical properties get involved. On those same mechanical properties, the drag zone tends to be wider and more intense on shale and clay-rich sequences than on massive competent units like sandstones and limestones (Fossen, 2020). The drag zone is separated into two main styles called *normal drag*, where the markers are convex to the direction of slip and the *reverse drag*, where the markers are concave to the direction of slip (Hamblin, 1965; Grasemann et al. 2005) (Figure 2.2). The appearance of a normal or reverse drag depends mainly on the angle between the fault and the markers, where a low-angle shows normal drag and a high-angle has reverse drag (Grasemann et al. 2005).
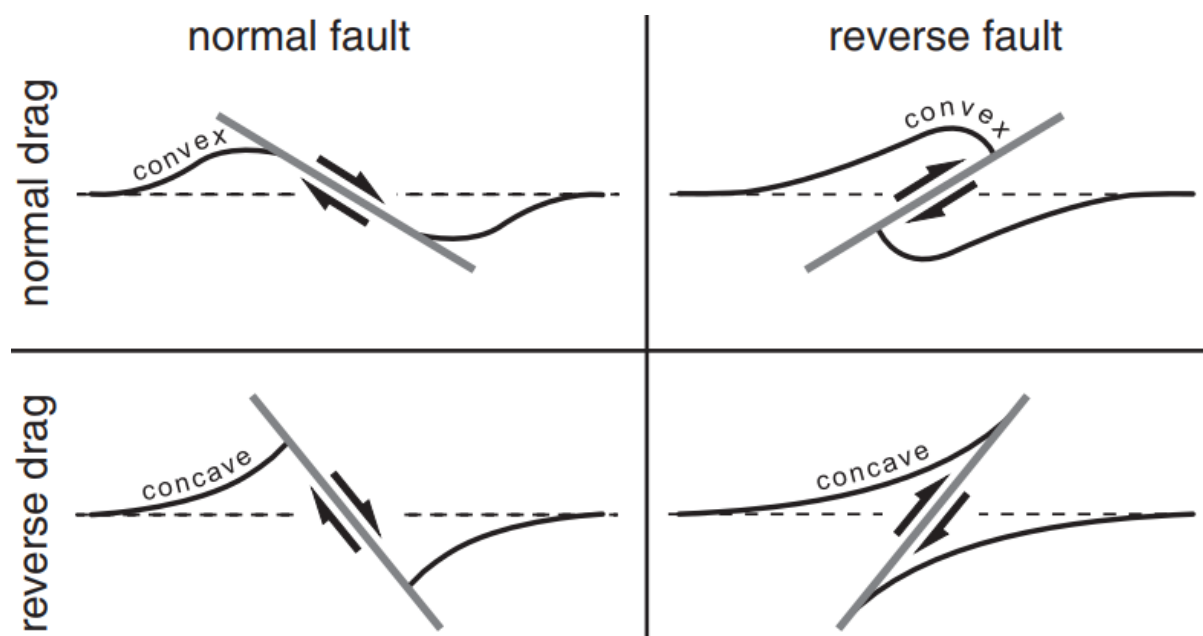
Figure 2.2: Examples of normal and reverse drag folds along normal and reverse faults. A normal drag fold is defined by it being convexly warped in the transport direction, while the reverse drag is the opposite. From Brandes and Tanner (2014), modified from Grasemann et al. (2005).

2.7 Fault lenses

Forming an integral part of the fault core or being a whole separated architectural element of a fault, depending on its size, a fault can contain smaller volumes of undeformed or less deformed host rock both within the fault core and in the damage zone (Lindanger et al., 2007; Braathen et al., 2009). The thickness of these lenses depends on the host rock's mechanical strength,

where poorly consolidated rocks tend to form thinner lenses and stronger rocks develop thicker ones (Lindanger et al., 2007). Lens structures can also have an important role in fluid flow, as their positioning may allow communication between reservoir units in the subsurface.

Figure 2.3: Hanging wall lens in the Bartlett normal fault containing a chunk of the Moab Mb. (white) and Slick Rock Mb. (Reddish/brown) of the Entrada Sandstone. Found in the Bartlett Wash Canyon in Utah, US.

2.8 Seismic acquisition and resolution

Seismic imaging is one of the most essential tools to characterize the subsurface in modern days. By using elastic waves, it is possible to understand how these subsurface rocks and their structures are positioned when they are not physically accessible by using rock physical properties in relation to this energy. When these elastic waves are applied to the rocks, the different properties between layers or structures may create variations in elastic impedance which act as boundaries where elastic energy will reflect back to the surface and be measured by geophones. This energy response is a function of the P and S wave velocities and the bulk density of the rocks in the subsurface, in addition to the incident angle. During seismic acquisition, multiple receivers will record each shot (**Error! Reference source not found.**),

recording reflections from different subsurface localities (Simm and Bacon, 2014). The next step is to stack all the individual traces recorded, summing the traces, which will, in turn, enhance the signal and suppress noise, forming a single seismogram. (**Error! Reference source not found.**). Each of these seismograms is itself a combined response of individual reflections generated due to localized variation in the elastic impedance (Figure 2.*4*).
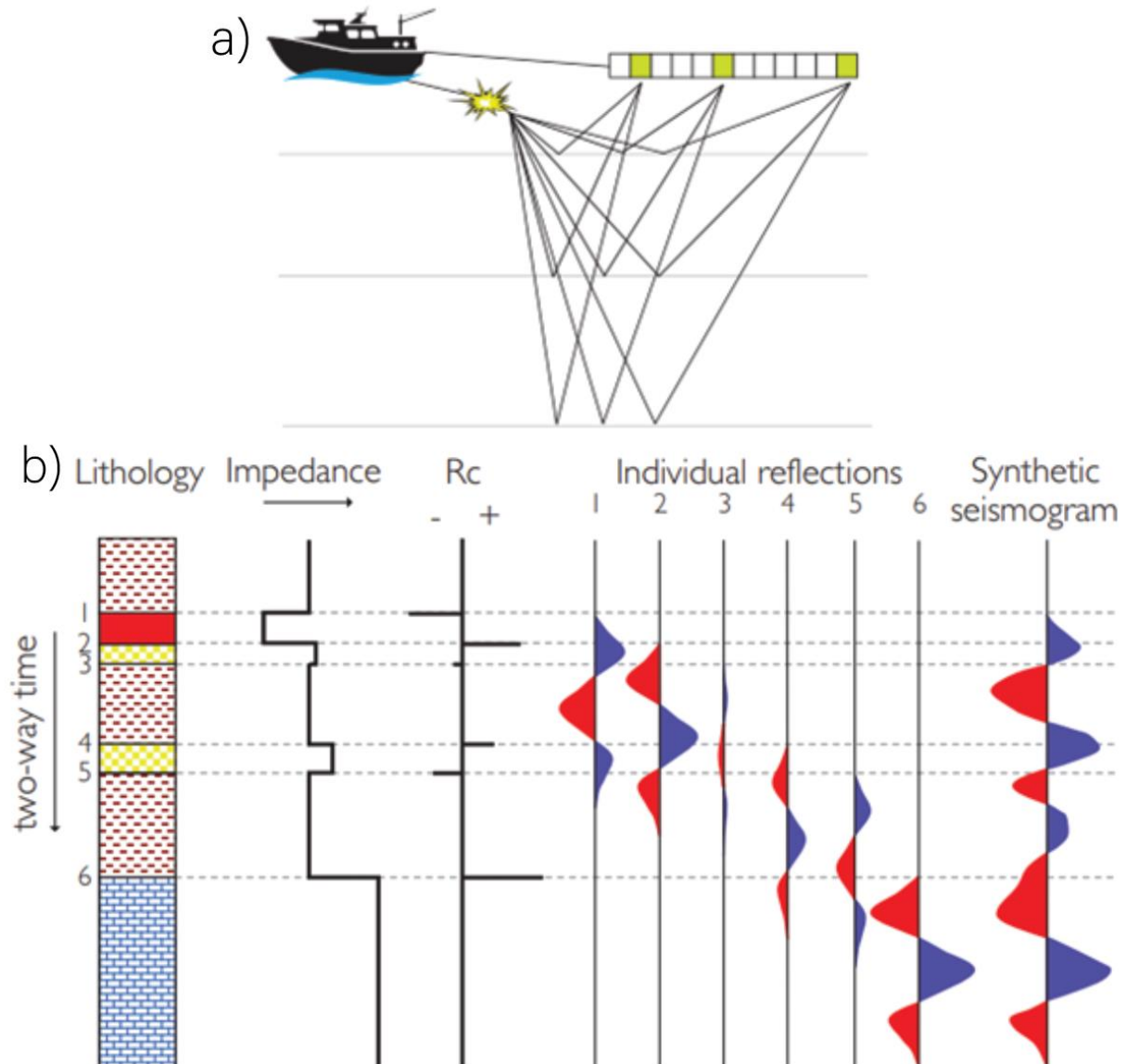
Figure 2.4: a) How data acquisition is made through a shot that multiple receivers wil. b) Illustration of different impedances and reflection coefficients induced by different lithologies and how the individual reflections are superimposed to form a single seismogram. From Simm and Bacon (2014).

In interpreting seismic images, one of the main challenges is the resolution of the image. This gets even more critical as the resolution puts a lower limit on the bed thickness that can be

imaged, creating uncertainty in the interpretation. The vertical resolution depends on the tuning thickness, which is determined by the wavelength of the seismic pulse (λ):

$$\text{Vertical resolution / Tuning thickness} = \lambda / 4$$

λ being a function itself of velocity and frequency:

$$\lambda = V/f \qquad \text{Equation 2.1}$$

The lateral resolution, which is not necessarily horizontal, is defined by the Fresnel zone, an area of the wavefront. Ideally, in a perfect illumination scenario, the lateral resolution would be the same size as the vertical one; however, since the standard illumination ranges between 40 – 50 deg in the steepest dip, when 3D migrated, the Fresnel zones will collapse into a small circle, with a diameter that is around half of the wavelength used (Simm and Bacon, 2014)

3.Moab Fault System.

The Moab fault system is an approximately 45 km long normal fault, extending north-west of the Moab-Spanish Valley Salt anticline, and located in the east of the state of Utah, US, inside the Paradox basin (Foxford et al. 1996; Davatzes & Aydin, 2005).

Q Quaternary eolian and alluvial deposits
Kmt Tununk Shale Mb of Mancos Shale
Kd Dakota Sst
Kcm Cedar mountain Fm
Jmb Brushy Basin of Morrison Fm
Jms Salt Wash Mb of Morrison Fm
Jsmt Tidwell Mb of Morrison Fm
Summerville Fm undivided
Jctm Moab Mb of Entrada Sst
Jes Slick Rock Mb of Entrada Sst
Jcd Dewey Bridge Mb of Entrada Sst
Jn Navajo SsT
Jk Kayenta Fm
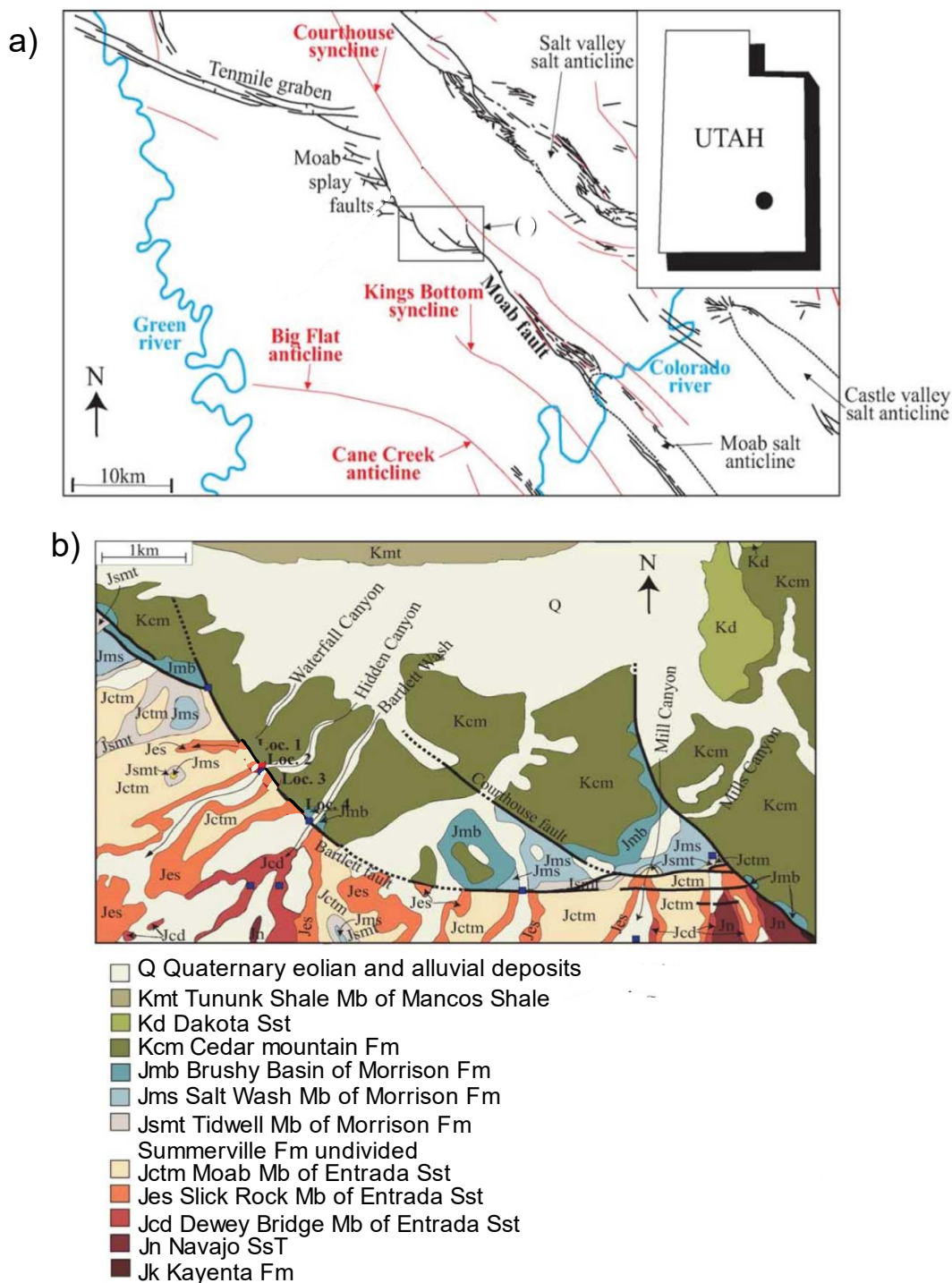
Figure 3.1: a) overview map showing the surrounding structures in the area around Utah. B) Geological map of the study area. Modified from Berg and Skar (2005).

With a maximum throw of ~950 m, the fault cuts through a sequence of Pennsylvanian to Cretaceous sediments, with this maximum throw appearing in the south, where the fault is related to an anticline. During the growth and linkage of these faults, the changes in the stress field created a range of deformation of structures such as deformation bands, striated slip planes and veins, all of which have a higher frequency close to those linkages (Davatzes et al., 2005; Johansen et al., 2005).

Due to its wide range in structural diversity and size, this well-exposed fault system was selected for the purpose of this thesis, as it possesses enough features that would have a significant impact on fluid flow and thus on the creation of reservoirs or ore deposits, and, through this, could serve as an analogue to larger structures imaged in the subsurface.

3.1 Courthouse-Bartlett Area Stratigraphy

Paradox Basin

Located in the Colorado Plateau in the western part of the United States, the Paradox basin started during the middle Pennsylvanian (~310Ma) as one of the intracratonic foreland basins to form due to a series of basement-cored uplifts known as the Ancestral Rocky Mountains (Doeling, 2001; Trudgill, 2001). In the Paradox basin case, the basin developed on the southwestern flank of the Uncompahgre uplift (Barbeau, 2003). With rocks with ages spanning from the Pennsylvanian to the Permian, the basin starts on the bottom with 2 to 2.5 km thick layers of evaporites of the Paradox formation that are topped by the Cutler Group, a heterogeneous sequence of arkosic sediments, deposited initially as alluvial fans and debris flow. (Foxford et al, 1996; Doelling, 2001).

Mesozoic Stratigraphy

As previously mentioned, the Moab fault cuts through a sequence of rocks spanning from the Pennsylvanian to the Cretaceous. However, for the purpose of this thesis, the Mesozoic sequences that are exposed near the fault segments of the north-west extension of the Moab fault are, according to Foxford et al. (1996) and Doeling (2002):

Navajo Sandstone (Lower Jurassic): An eolian-dominated sequence with light fine to medium-grained, eolian sandstone; locally contains thin, hard, grey limestone beds. Has an average thickness of 40 to 50 m.

Entrada Sandstone, Dewey Bridge Member (Middle Jurassic): The lowest member of the Entrada Sandstone, the lower half is an interbedded dark-red, red-brown, light-brown, and

yellow-grey, fine to medium-grained sandstone, and is commonly calcareous and cherty. The upper half is a dark-red, muddy, earthy, fine-grained sandstone, commonly contorted, nodular, or having indistinct bedding. Has an average thickness of 40 to 60 m.

Entrada Sandstone, Slick Rock Member (Middle Jurassic): Mostly orange-red or banded orange-white sandstone, fine-grained, eolian sandstone. The lower contact with the Dewey Bridge member is commonly crenulated or contorted. Has an average thickness of 55 to 65 m.

Entrada Sandstone, Moab Member (Middle Jurassic): Light-yellow-grey, fine to medium-grained, cross-bedded, massive sandstone, with interbedded aeolian interdune and dune at the base and large dune sets at the top. The sandstone in this unit is more well-sorted and contains fewer fines than the Slick Rock member. Has an average thickness of 25 to 30 m.

Curtis Formation (Middle Jurassic): Brown, grey, green, lavender, and orange interbedded siltstone and fine-grained sandstones. Siltstones are mostly thin-bedded, argillaceous and calcareous. The sandstones were deposited on a wave-reworked, sand-dominated sabkha. Has an average thickness of 0 to 10 m.

Morrison Formation, Tidwell Member (Upper Jurassic): A calcareous, thin-bedded lavender, marron, and light-grey siltstone, light-grey, thin to thick-bedded, very fine-grained sandstone, and grey thin-bedded limestone. Has an average thickness of 10 to 15 m.

Morrison Formation, Salt Wash Member (Upper Jurassic): Light-yellow-grey, fine to coarse-grained, forming medium to thick lenses sandstone interbedded with red and grey mudstone and siltstone. Has an average thickness of 60 m

Morrison Formation, Brushy Basin Member (Upper Jurassic): Variegated mudstone interbedded with grey, white, or brown conglomeratic sandstone, conglomerate, nodular limestone, and gritstone. Outcrops are generally prone to slumping. Has an average thickness of 80 to 90m.

Cedar Mt. Formation (Lower Cretaceous): Drab olive-green to variegated mudstone and brown to grey sandstone, gritstone, conglomerate, and limestone. The lower contact with the Morrison Fm. is placed at the base of a prominent sandstone or conglomerate ledge or cliff. Has an average thickness of 30 to 60 m.

(Stratigraphic thickness from Foxford et al., 1996)

3.2 Moab Fault Tectonics

The segmented Moab fault system initially formed as a result of the rapid salt diapirism of the Paradox Formation, with the southern portion of the Moab fault being along the southwest limb of the Moab-Spanish Valley salt anticline. Foxford et al. (1996) suggest that the fault had two main phases of activation, where the first phase of displacement occurred during the Triassic to Lower Jurassic and the second phase of displacement happening between around 60 Ma, according to clay mineral dating (Solum et al., 2005). These two phases have been associated again with salt movement during the Laramide orogeny and inversion of the Paradox basin. respectively (Doelling, 1988; Davatzes & Aydin, 2003).

4.Seismic Modelling

Seismic modelling is a method simulating elastic-wave propagation in the subsurface of the earth (Carcione et al., 2002; Lecomte et al., 2015). By simulating these waves in different numerical/analogue models, it is possible to compare them with real seismic data collected worldwide. This comparison allows us not only to validate geological models, but also to increase our understanding of the limitations and potential pitfalls of seismic data. This chapter will focus on the theory behind the modelling method used in this thesis, and the seismic variables that could affect the imaging of faults and their zone of influence.

4.1 Main Modelling Approach

As seismic modelling has become more sophisticated and realistic, several different methods have been developed, each with its strengths and limitations that make them more or less appropriate for each specific case. The one considered to be the most adequate for this thesis is a 2(3)D convolution modelling making use of ray-based (RB) generated Point-Spread Function (PSF) i.e., point-scatterers responses of seismic imaging. This method modelled directly Prestack Depth Migration (PSDM) sections (Lecomte, 2008; Lecomte et al., 2016). In the RB method, the most standard method would be to use the 1D convolution method, where each seismic trace of a model is generated individually but, although the vertical resolution is properly estimated, the lateral resolution effects are not considered, as well as limited illumination issues, thus generating incomplete modelling results especially when lateral velocities variations are expected (Lecomte et al., 2015). A PSF-based convolution modelling does include lateral resolution and limited-illumination effects in such cases.

Another alternative is to use a Full-wavefield (FW) method, which generates complete synthetic seismograms containing all wave types (e.g. headwaves, surface waves, diffractions, etc), thus producing more realistic synthetic records. However, such methods are much more resource- and time-consuming, both in calculating synthetic seismograms and then processing the latter to produce a similar PSDM image (Lecomte et al., 2015; Jensen et al., 2021). In the present modelling work, the need for various sensitivity analysis required a more efficient method even if less complete and producing near-ideal PSDM images (i.e., without the possible impact of multiples, waves conversions, etc)

4.2 PSF-based 2(3)D convolution modelling

In this method, 2(3)D spatial convolution operators, called Point-Spread Functions, are first generated via, e.g., RB information or a few key parameters, then used to simulate PSDM images (Lecomte, 2008; Lecomte et al., 2016). The method distorts in essence the actual reflectivity to reproduce the effects of seismic imaging, each reflectivity element of the input model acting as a point scatterer. The modelling image thus results from the combined interference of all point-scatterers responses (i.e., as modelled by the PSF), including limited illumination effects (e.g., steep reflectors not part of the image).

To generate an image with this method, the first step is to calculate so-called Illumination vectors for each shot (S) and receiver R pair (I_{SR}). To do so, two slowness vectors are estimated (RB), one attached to the incident wavefield (i.e., towards S; p_S) and one to the scattered wavefield (i.e., towards R; p_R), this in a given velocity model (Lecomte, 2008):

$$I_{SR} = p_R - p_S$$

Both its orientation characteri (as a combination of its incident and scattered wavefields) and length (function of the velocity at the considered reference point and the opening angle between p_R and p_S), with these two completely controlling the illumination and resolution in a PSDM image. A reflector is illuminated as long as its normal is parallel to one of the available I_{SR} directions. The next step is generating scattering wavenumbers and mapping them into the wavenumber domain to generate PSDM filters, which in turn yield the PSF after a Fourier Transform to come back to the spatial domain (Lecomte 2008).

PSDM images are finally generated by convolving the PSF with reflectivity structures mapped on a grid. This method could be applied to both 2D and 3D structures. However, due to a lack of information between some of the studied profiles, it would have been difficult to build detailed 3D geological models, and it was thus decided that only 2D cases would be modelled.

4.3 Analytical PSF

As described above, the key element to conducting the 2(3)D convolution modelling is that the PSFs can be generated based on RB information collected from a background velocity model and survey geometry. However, when this information is not available or limited, it can be produced analytically. Such a generic-PSF approach starts by defining the average velocity of

the targeted model, an incident angle (θ), and a maximum illumination angle, as well as selecting a wavelet describing the frequency content of the considered seismic signal. These parameters will affect how the simulated seismic image will appear, as would be the case with actual seismic.

As mentioned before, geological structures are only being imaged if their dips are covered by the PDSM filter, i.e., being parallel to I_{SR}. When using generic PSF, the user just defines the steepest illuminated reflector dip. In Figure 4.1, a PSDM filter with its corresponding PSF has been designed for a maximum illumination angle of 45°; in this example, no geological structure with a dip higher than 45∘ would be imaged on the seismic data. In the corresponding PSF, a cross pattern due to the truncation effects in the wavenumber domain is visible, thus showing the maximum illumination angle. For the sake of understanding illumination impact, the maximum illumination angle can be set to whatever value one wishes, including 90°, thus, being able to image all ranges of geological dips in a set model. This scenario is called "Perfect Illumination" being mostly a theoretical scenario since it is nearly impossible to obtain it in real seismic. Indeed, the maximum illumination angle in standard 3D seismic rarely goes beyond 40°-50° dip.
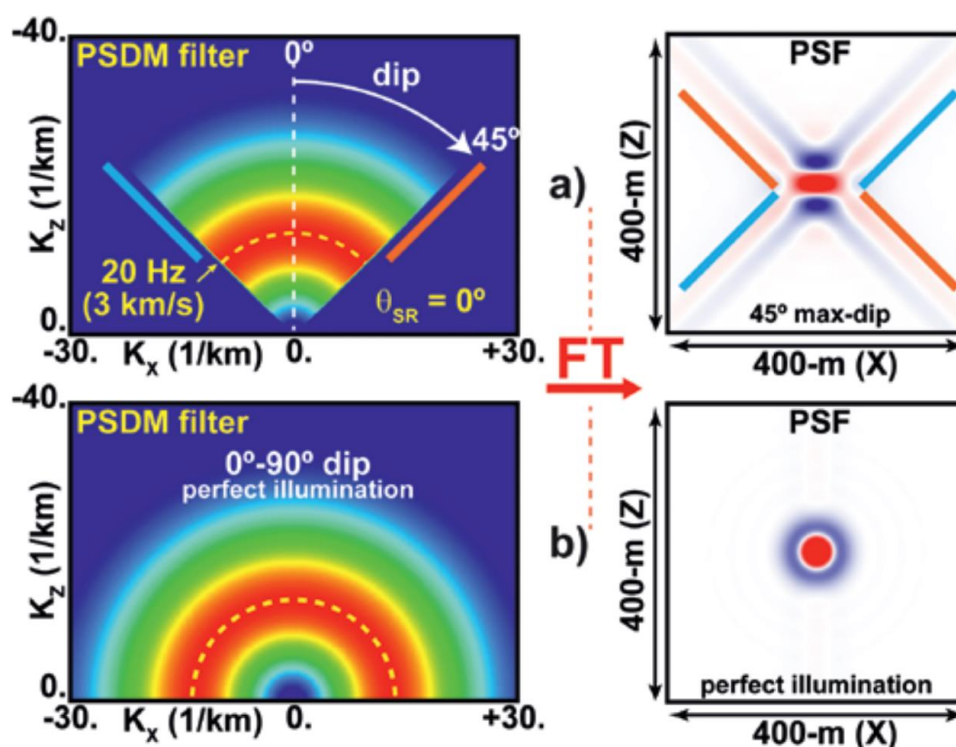
Figure 4.1: a) To the left is the PSDM filter with a velocity of 3 km/s, the incident angle of 0°, 20-Hz frequency and a 45° illumination angle, and to the right is the PSF with resolution and cross-pattern from dip limits of the previous image. b) Same PSDM filter but with a perfect illumination (90°) and its PSF on the right. Extracted from Lecomte et al. 2016.

5.Data and Methodology

The following chapter outlines the methodology used in this thesis, with information on the software and fieldwork necessary and the steps taken in each process. This thesis produced geological models based on real outcrops in the Moab Fault region (Utah, US) with information obtained through fieldwork or Virtual Outcrops (VO) in LIME. These geological models produced with Adobe Illustrator and MATLAB were used in SeisRoX to create 2D Synthetic seismic. Those were compared with real seismic data that were analysed and processed in Petrel.

5.1 Virtual Outcrops and LIME

As previously explained, Virtual Outcrops (VOs) have advantages such as allowing for extensive coverage of large areas while maintaining a high-resolution level. This thesis used two VO, available on the V3GEO website (www.v3geo.com): The VO for the Courthouse and Bartlett canyon in Utah, US. The first one covers an area of roughly 0.3 km^2, showing the north side of the courthouse canyon, with good exposition and easily observable of its stratigraphy, and the abutting of the Moab and Courthouse faults. The Bartlett VO covers an area of 1.2 km^2, showing the Bartlett Wash Canyon, with a good exposition of its stratigraphy, an excellent exposition of the fault core and a small area of the hanging wall. The resolution of both VOs is informed to be around 20 cm.

To properly interpret those VOs, a software focused exactly on this task, known as LIME, was used. Both VOs were directly imported into the software using the software's own function to import VOs from V3GEO and interpreted using the "3D element" tool to highlight stratigraphic and structural features found on the outcrops. These tools, combined with the possibility to create a 2D panel that creates an image of both the VO and the 3D elements created, allow high-resolution models based on those 2D images.

5.2 Fieldwork

As the VOs were limited both in resolution and coverage, there was a gap in information in the field area, with this gap being more evident in the other canyons in the area. Fieldwork was carried out from the 06th to the 14th of May 2022 in the northern part of the Moab fault system between the cities of Green River and Moab, Utah. The main objectives of this fieldwork were

to explore and collect detailed data from inside and around the canyons in the previously mentioned area, as they represent excellent outcrops, with some of them almost producing a partial profile of the stratigraphy and structures found around the faults. The canyons in the area are disposed from east to west as follows: Courthouse, Mill, Tusher, Bartlett, Hidden and the Waterfall canyon. All canyons are located within an area of ~25 km^2.

During the fieldwork, structures found inside and around the canyons were measured, and the walls and surroundings of the canyons were photographed. For the structures measured, there was an emphasis on measuring faults and deformation bands found along its extension. Field equipment used were: Compass, a geological hammer, measuring tape, a mobile phone camera and the app "Clino". Most of the canyons were easily accessible by car or close enough to require just a small hike or climb. In a few places, the outcrop and its structures were covered by scree, in areas of difficult access or with a chance of rock fall. However, most places had the structures easily accessible or at least observable.

5.3 Well data and elastic properties

With the geological models created, elastic parameters were necessary to transform these simple geometric models into seismic ones. As a basis for these values, data from the North Sea Well 34/10-41S (Table 5.1) and Stockton & Balch (1978) (Table 5.2) were used to fill in this information. The values obtained in Stockton & Balch (1978), although having data from the units the models were based on, were not from specific units most of the time, grouping together many members of a single formation in a range of P-wave velocity (Vp) values. For the Vp values used from the Stockton & Balch (1978) case, the Vs values were estimated based on a constant Vp/Vs ratio: Vp/2 (Faleide et al. 2021). The North Sea Well data were accessed from the DISKOS database to which the University of Bergen (UiB) has an open-source access agreement and was chosen because they cover the Heather Fm. and the Brent Gp. The elastic data for these units are within the same range as that presented in Stockton & Balch (1978).

34/10-41 S Elastic Parameters					
Formation	Density (g/cm^3)	P-wave velocity (us/ft)	P-wave velocity (km/s)	S-wave velocity (us/ft)	S-wave velocity (km/s)
Heather Fm.	2.29	112.8	2.7	248	1.2

Tarbert Fm.	2.46	72.5	4.2	170.5	1.8
Ness Fm.	2.26	107	2.8	202.3	1.5
Etive Fm.	2.15	105.8	2.9	200.7	1.5
Rannoch Fm.	2.3	97.4	3.1	192.8	1.6
Broom Fm.	2.38	109.5	2.8	230.6	1.3
Below Brent average	2.25	92.1	3.3	201	1.5

Table 5. 1: Elastic parameters for density, P-wave and S-wave velocity (in us/ft and km/s), for the Heather Fm., the formation in Brent Group and average values for layers below, measured from the well 34/10-41 S

Stockton & Balch (1978) Seismic survey		
Units	Density (g/cm^3)	P-wave velocity (km/s)
Brushy Basin Mb.	2.29 – 2.35	3.275 – 3.4
Salt Wash Mb		
Moab Mb	2.35 – 2.49	3.1 – 4.25
Slick Rock Mb		
Dewey Bridge Mb.		

Table 5. 2: Elastic parameters for density and P-wave velocity for the units worked in this thesis found in Stockton & Balch (1978).

5.4 2D Seismic modelling

With the geological models created from the virtual outcrops or from the description and photos of outcrops during the fieldwork, it is necessary to merge the model's image with elastic properties information so the result can be processed in the software that will generate the synthetic seismic. The first step is to populate the model with these elastic parameters through a MATLAB script. The parameters used were Vp, Vs, and Rho (density). In addition, a random white reflective grid was generated to be able to add noise to the synthetic seismic.

After converting each grid of elastic parameters and noise to the SEG-Y file format, they were imported to SeisRoX. Following a reasonable standard 3D-seismic illumination, the maximum illumination angle was set to 45° (Simm & Bacon, 2014). An average velocity of 3.1 km/s was estimated for the targets of interest. The input wavelets chosen for testing the resolution were: 10 Hz, 20 Hz, 30 Hz, 40 Hz (representing conventional seismic), and 100 Hz (representing high-resolution seismic). To verify how the size of the units and structures would

impact the resolution of the seismic image, models with the base size (100 m), 5x upscaled, and 10x upscaled were produced. The range of all parameters used can be seen below:

- Dominant frequency (Hz): 10, 20, 30, 40 and 100
- Maximum illumination angle (°): 30, 45, 60 and 90
- Level of Noise (%): 0, 25, 50, 75 and 100
- Incident angle (°): 0, 20 and 40
- Size: original, 5x and 10x upscaled

5.5 Workflow
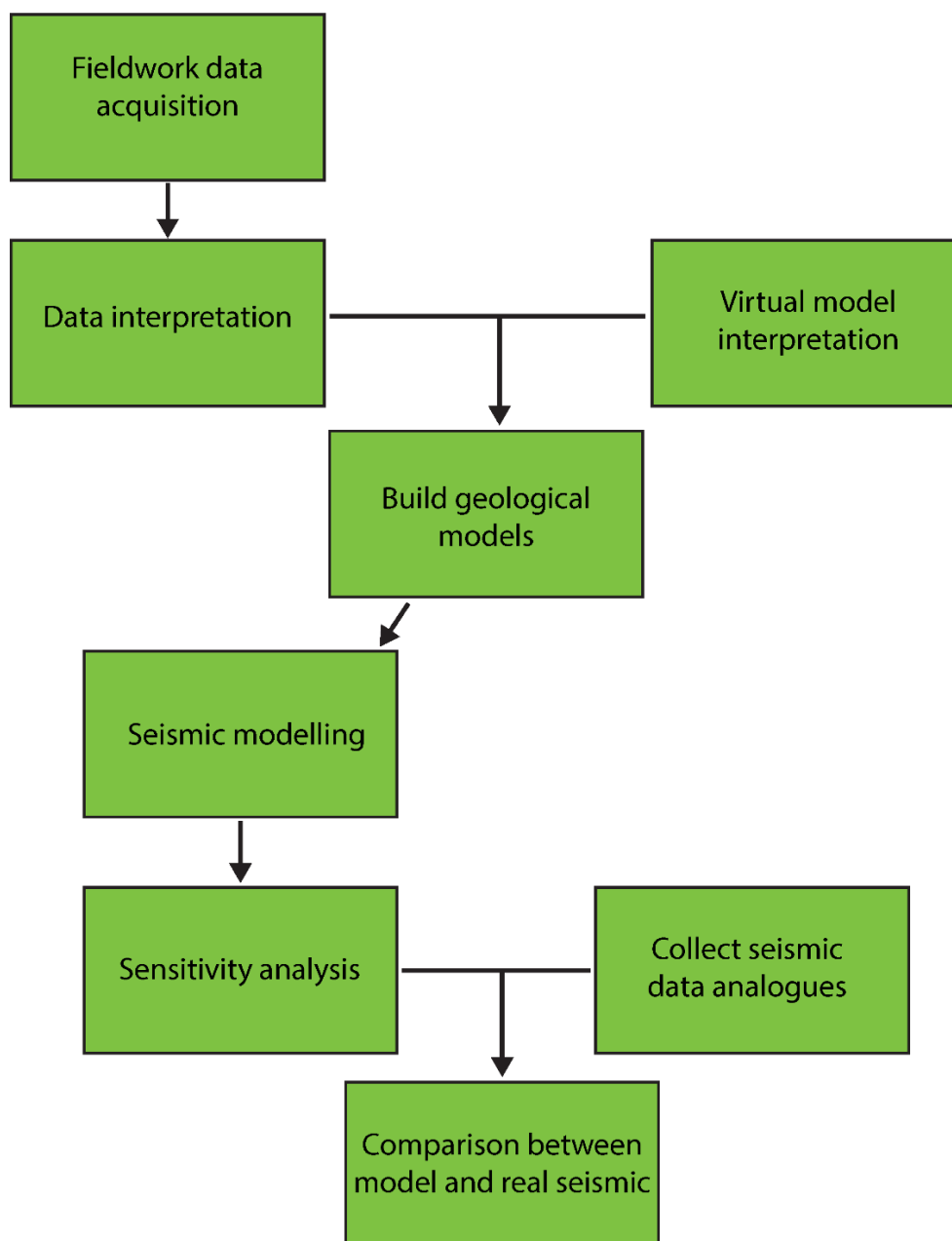
Figure 5. 1: Workflow chart illustrating the workflow conducted in the thesis

6.Results

This chapter presents seismic modelling results, as obtained through the methodology presented in the previous chapter. Geometric 2D modelling of the canyons around the Moab Fault Splays was based on the virtual outcrop models or data collected during fieldwork. Later, synthetic seismic modelling was generated based on these geometric models.

The synthetic seismic models used in this thesis have no vertical exaggeration (VE 1:1); the vertical axis is always in depth (unlike what often is the case with actual seismic data), and all results are proxies of PSDM images.

6.1 Moab fault splay canyons geology

Towards its northwestern termination, the Moab Fault splays into a set of smaller faults with somewhat different orientations (Doelling, 2002). The Jurassic section of these splay faults was exhumed during the Late Cretaceous to Quaternary uplift of the Colorado Plateau, and associated erosion has created six large canyons that cross the fault trend, exhibiting much of the local stratigraphy in well-exposed steep to vertical walls. In general, the degree of exposure is better in the footwall because of the more weathering-resistant Entrada Sandstone. In contrast, the easily erodible mudstones of the Morrison and Cedar Mountain formation are less well exposed.

The stratigraphy and structural data collected from both the virtual outcrops and fieldwork are summarised below for each of the canyons, starting from the canyon closest to the intersection between the Moab and Courthouse faults and moving successively to the northwest:

6.1.1 Courthouse Canyon

The first canyon on this list is also the deepest, with around 100 meters tall walls. In the footwall, all units of the Entrada Sandstone are exposed. From top to bottom, the Moab Mb. appears above all other units in the footwall, probably partially eroded. Beds of the Slick Rock Mb. are mostly planar but in a few areas of contact with the Dewey Bridge Mb. they form dome-like structures, mainly on the canyon's east side, close to the fault. Beyond that, the Dewey bridge Mb. slowly surfaces as planar beds southwards into the canyon, as the stratigraphy here has a light 6° NW dip (Foxford et al. 1996), a trend that follows most of the canyons in this

thesis. Due to this tilt, around 400 meters south fault, there are outcrops of the underlying Navajo Sandstone further into the canyon.

On the hanging wall to the east, there is a triangular outcrop of the Moab Mb, edged exactly between the intersection of the Moab and Courthouse faults, and would connect with the east side of the canyon if not for an erosive gap that removed 100 meters of this side of the canyon. Going westwards, the Morrison Fm. surfaces, with the Tidwell member mostly covered by scree and appearing primarily through differences in soil colour, and the Salt Wash Mb and its sandstone lenses.

As the Courthouse Canyon is the closest canyon to the abutting of the Moab and Courthouse faults, this is also the canyon with the higher number of deformation structures. The Courthouse Fault cuts this area with an average northward dip of 72° and has a displacement varying between 60 to 90 meters, from closest to furthest away from the abutting of Moab and Courthouse fault, based on the stratigraphy and previous works. There is the presence of deformation bands in the vicinity of the fault. South into the canyon, the area has another four smaller faults with less than 10 meters of offset, two dipping southwards and the other two northwards. On the east side of the canyon, all faults are distant from one another; however, on the west side, the second and third are united halfway through the outcrop. This also makes for the appearance of multiple sets of much smaller faults in the surrounding area.

6.1.2 Mill Canyon

With roughly the same size as the Courthouse Canyon, Mill Canyon's stratigraphy has few differences compared to the Courthouse one. On the footwall, the stratigraphy follows the same as the previous is, but without the presence of the dome-like structures and the Dewey Bridge Mb. Near the fault and the presence of a few meters layer of the Curtis Fm. The only unit visible on the hanging wall is the Salt Wash Mb. of the Morrison Fm.

The Courthouse Fault in this area starts to change its direction and go northwest. Here the fault has an average dip between 65° to 70°NW, while the displacement is around 100m. The courthouse Fault is accompanied by a parallel second fault, with the same dip direction and angle, less than 10m apart on the east side and around 20m on the west side. A third smaller fault, with a displacement of about eight meters and a 70°N dip, is found further south into the canyon.

6.1.3 Tusher Canyon

The Tusher Canyon, unlike the other areas, only has its east side of the fault crossing visible, as the west side was completely covered in soil and scree. The stratigraphy still followed the same trend as the previous areas but with the lack of the Dewey Bridge Mb. this time. The hanging wall is still composed of the Morrison formation, with ticker layers of sandstone (>10m) in this area.

The fault in this canyon is the only major fault in the area, with a dip of around 80N° and an offset of around 100 meters. The outstanding feature of this fault is the presence of a large lens of the footwall containing a series of minor faults exposed on the east side outcrop. The fault at the top of this lens has a lower angle, raising the question if this is only a lens or a relay zone created by two separated faults.

6.1.4 Bartlett Canyon

From Bartlett Canyon onwards, the canyons mentioned here are pointing northeast, following still perpendicular to the fault, this time the Bartlett Fault, which the strike points northwest. Bartletts Canyon stratigraphy on the footwall keeps the same trend as the previous canyons, where the Moab Mb. is on the top, slightly eroded, followed by a large exposition of the Slick Rock Member. Further into the canyon is a small exposition of the top of the Dewey Bridge Member. On the hanging wall, the Brushy Basin Mb. of the Morrison Fm. is exposed at the bottom, while the cretaceous Cedar Mountain Fm. is above.

Bartlett Fault crossing of this canyon is marked by a northeast dip of 68° with a displacement of 210 and a series of large fault lenses, being 5 to 25m wide and having more than 100m of length for the largest, on both sides of the canyon. They all have a small displacement (<10m) compared to the main fault.

6.1.5 Hidden Canyon

Hidden Canyon stratigraphy follows almost the same stratigraphy as the one found in Bartlett. The footwall only has outcrops of the Moab and Slick Rock members, while the hanging wall has only outcrops of the Cedar Mountain Fm.

The fault crossing this canyon has a northeast dip of 62° and a displacement around 220 meters. Beyond the presence of deformation bands, this canyon's southeast side lacks any other major subsidiary structures. On the northwest side, two sandstone lenses from the footwall are present, being 5 to 10 meters wide and with a length of up to 50 meters.

6.1.6 Waterfall Canyon

Waterfall Canyon stratigraphy follows the same stratigraphy found in Hidden Canyon. The footwall is composed of the Moab and Slick Rock members, while the hanging wall is composed of the Cedar Mountain Fm.

The fault crossing the canyon was not properly measured due to difficulties in access to the area, but both sides seemed to follow the same trend in dip angle and direction and fault offset as the previous faults. From a distant observation, no other deformation structure was present beyond the main fault.

6.2   North Sea seismic

North Sea seismic images were collected from data ceded by CCG, from an area of around 44.800 km^2 on the west coast of Norway (Figure 6.1). The objective was to find faults and related deformation structures that could be compared with the synthetic seismic images produced from the field examples to compare both images and get further insight into how structural details and complications may or may not be imaged and how to avoid problems that may arise from it.
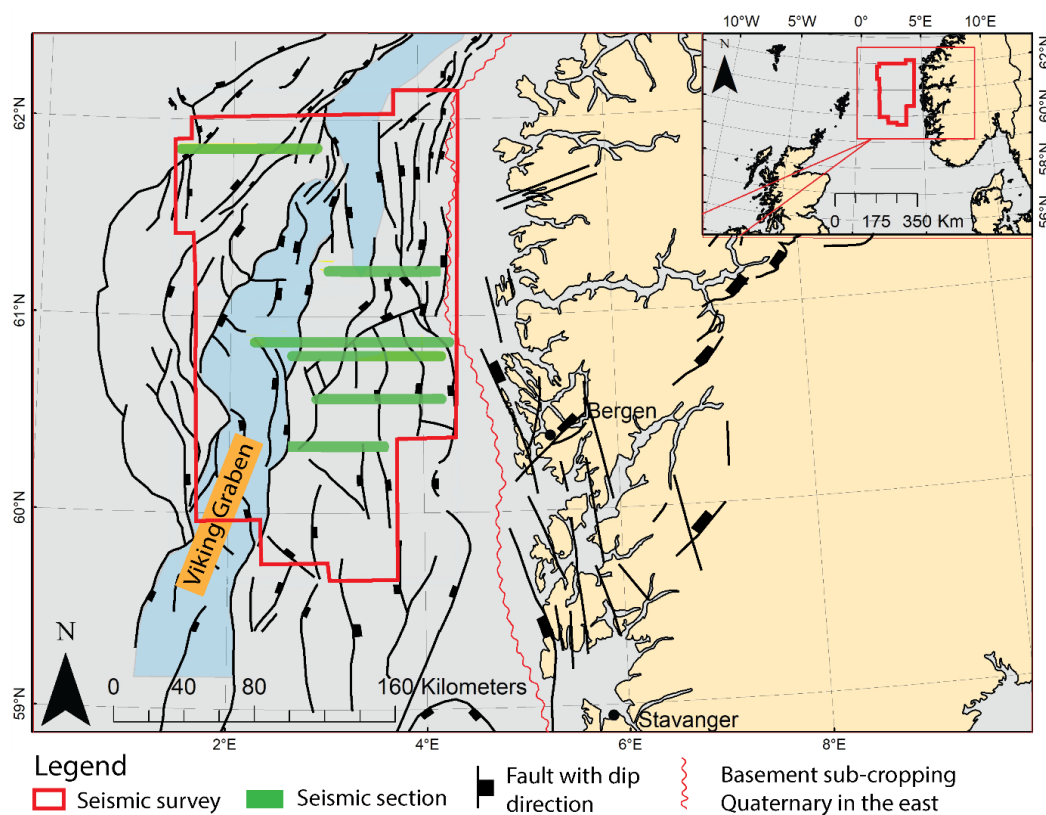
Figure 6.1: Map showing the area covered by the seismic survey used in this thesis, along with the major faults in the area and the position for some of the seismic sections used in further chapters. Modified from Bauck et al., 2021.

As the region is composed of a series of normal faults with a North-South strike, the image extracted from this data has an East-West direction to crosscut the structures in this region. Most of the seismic images that will be discussed here are present in Figure 6.2, along with a map of the region with an approximate position from where these images were extracted. The images cover a large range of sizes and structures and has a VE of 5:1. As expected from normal faults, many of the structures previously mentioned in Chapter 2 are visible in them. These structures being properly imaged or not and the impact they may have in interpretations and modelling of seismic images will be discussed in the next chapter.
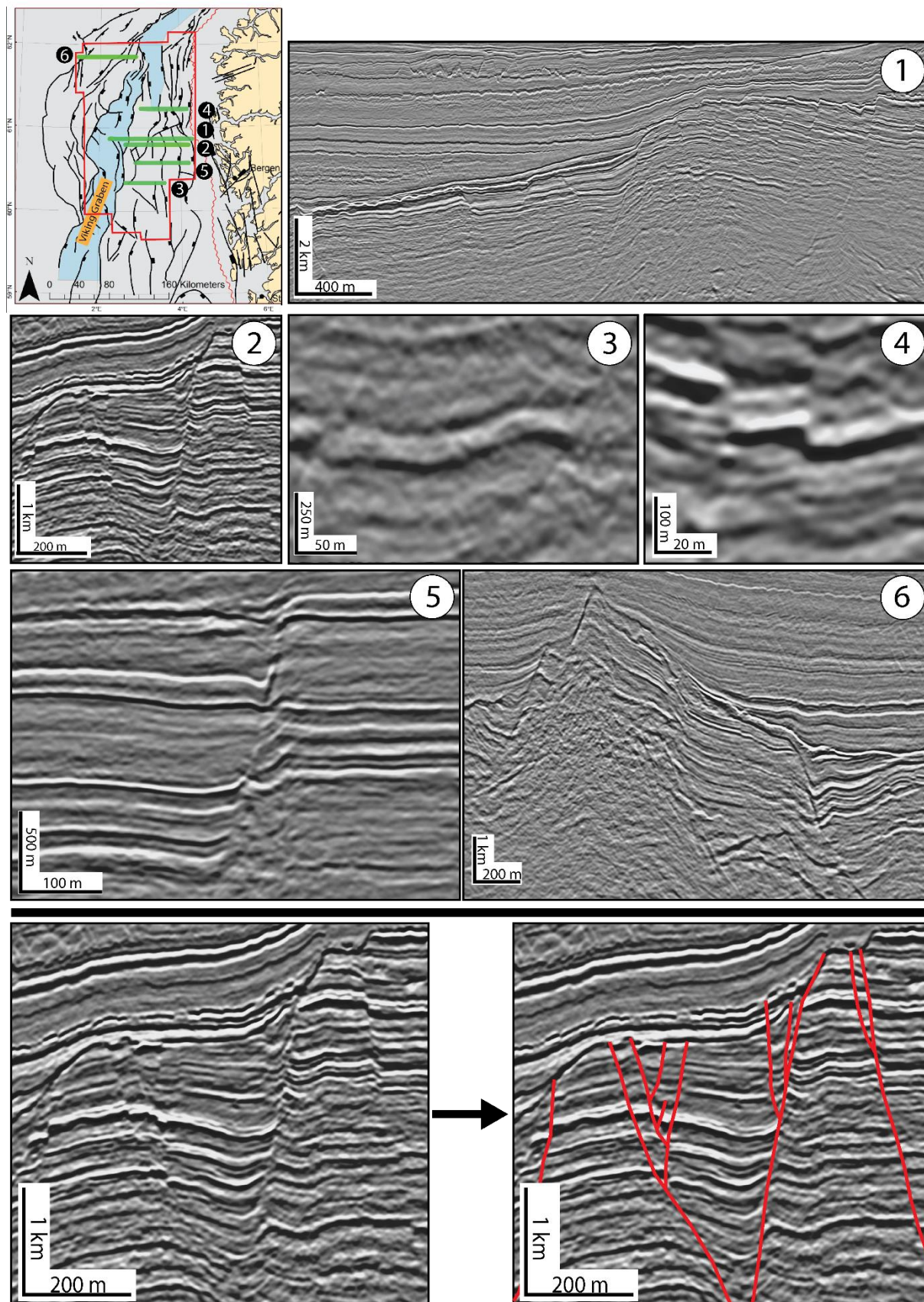
Figure 6.2: Seismic sections extracted from the seismic survey used in this thesis. All of them show sets of normal faults of different sizes and displacements with the position of these sections in the map in the top left corner.

6.3 Seismic Modelling Results

Faults on seismic data can be of great importance as the offset is capable of juxtaposing different layers. In the outcrops chosen for seismic modelling, the different displacement ranges and the subsidiary deformation structures allow these different properties to interact, creating seismic signatures that could be compared to real seismic data acquired from the North Sea.

Following the presets explained in Chapter 6, seismic models from the outcrops available in the canyons were built. As the outcrops studied had somewhat different heights, ranging from 80 to 100 m, and setting different project folders for each one would be very time-consuming, a height of 100 m was established as the basic height for all the outcrop models in the seismic modelling. Since all these outcrops belong on the same order of magnitude, modifying their height to the chosen set number would have a low impact on the final result.

The units were subdivided following Doelling (2002) and Foxford et al. (1996), as explained in Chapter 2. The only deviation from their subdivision was the Slick Rock Mb of the Entrada Fm., The Salt Wash Mb. of the Morrison Fm and the Cedar Mountain Fm., as these units had visible subunits of mudstone and sandstones for the Salt Wash Mb. and the Cedar Mountain Fm. and dune and interdune sub-units in the Slick Rock Mb. The other units interpreted in the models were massive, in the subsurface, or eroded. Due to the lack of accurate data, the models interpreted units in the previously mentioned conditions as massive. For the elastic properties used for each unit in the models, the values were chosen depending on how close the lithologies from 34/10 31 S well and lithologies descriptions from the units detailed in chapter 3. For units whose lithology didn't match as closely and had values available from Stockton & Balch (1978), the latter was chosen over the well data. The values chosen for each unit can be seen in Table 3. For the colour map for the seismic models, a white-gray-black scale with a 50% amplitude clipping was chosen to get as close as possible to the North Sea seismic data used in this thesis

Elastic properties in models				
Unit	Density (g/cm^3)	P-Wave velocity (km/s)	S-Wave velocity (km/s)	Reference Unit
Cedar Mountain Fm. (Mdst)	2.29	2.7	1.2	Heather Fm.
Cedar Mountain Fm. (Sdst)	2.3	3.1	1.6	Rannoch Fm.
Brushy Basin Mb.	2.35	3.4	1.7	Stockton & Balch (1978) values
Salt Wash Mb. (Mdst)	2.29	2.7	1.2	Heather Fm.
Salt Wash Mb. (Sdst)	2.29	3.3	1.65	Stockton & Balch (1978) values
Tidwell Mb.	2.46	4.2	1.8	Tarbert Fm.
Moab Mb.	2.29	3.1	1.55	Stockton & Balch (1978) values
Curtis Fm.	2.38	2.8	1.3	Broom Fm.
Slick Rock Mb. (Id)	2.26	2.8	1.5	Ness Fm.
Slick Rock Mb. (D)	2.15	2.9	1.5	Etive Fm.
Dewey Bridge Mb	2.25	3.3	1.5	Below Brent

Table 6 1: Elastic properties values and the units used to produce the synthetic seismic models.

The canyons used as the geometric basis for the synthetic seismic sections have a diversity of deformation structures, ranging from areas with a high to a low number of these structures. As explored below, this can deeply impact the images produced, leading from a simple and easily interpretable fault seismic scenario to more complex and challenging images. For the next two sub-sections, the seismic parameters used to model the images were: Dominant frequency of 30 Hz, Illumination angle of 45°, incident angle of 0° and the level of noise at zero. The dominant frequency and illumination angle values were set to be intermediary values, while the values for the incident angle and the level of noise were set to zero so to produce cleaner images. Of the parameters values chosen, their variation will be later discussed in sub-section 6.3.3.

6.3.1 Simple fault geometry

Areas like the Waterfall and a close-up of the main fault on Courthouse Canyon have very simple, planar fault structures, lacking the larger structures that could further impact the seismic imaging. Nevertheless, they still juxtapose different units with different elastic properties and show other deformation structures like drag which can be observed in the images below.
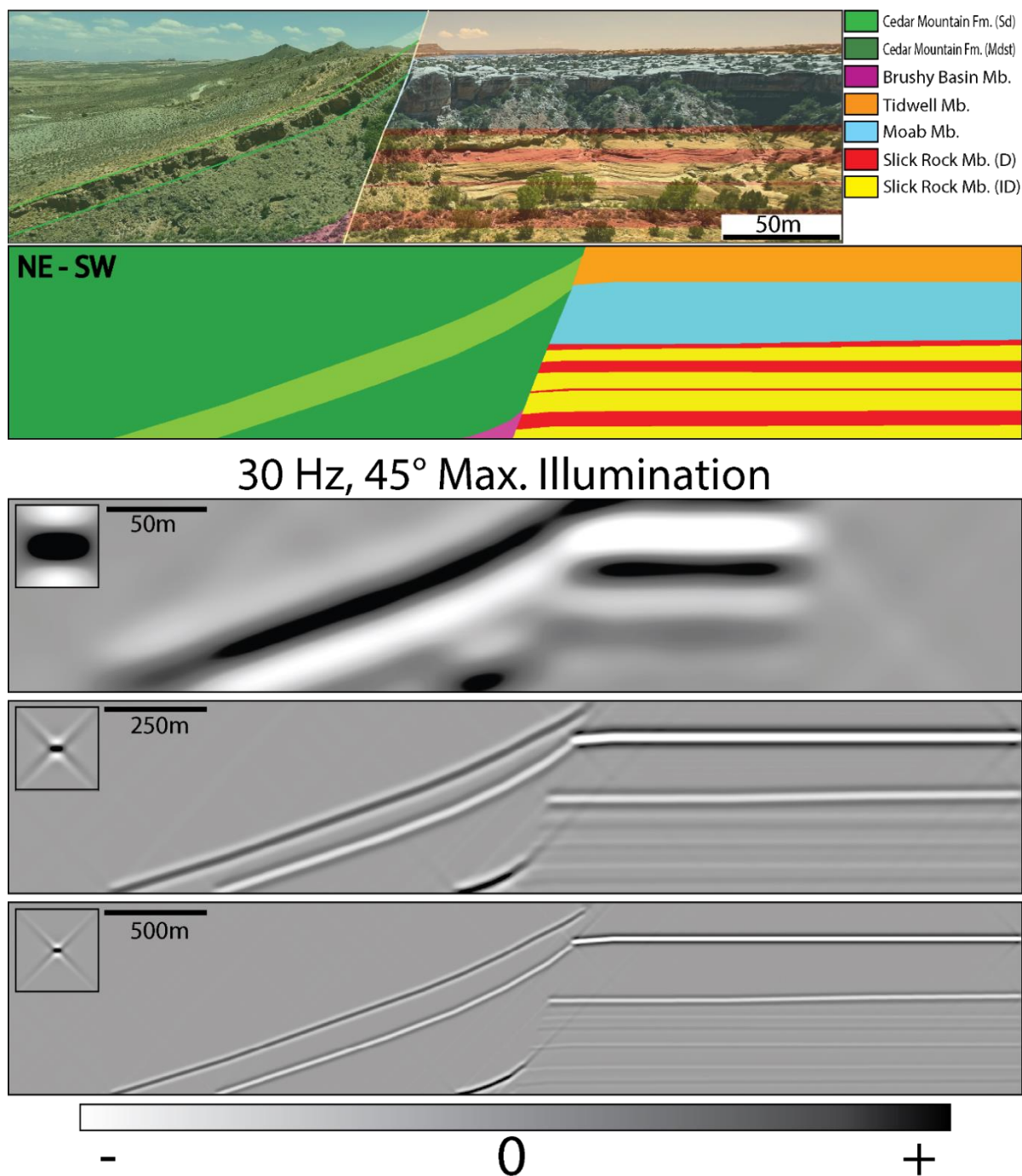
Figure 6.3: Synthetic seismic analysis of a simple fault at the southeastern wall of Waterfall Canyon. A normal fault runs through the area, juxtaposing Jurassic sandstones against Cretaceous beds. The model upscaling increases from top to bottom, the real size to ten times upscale, increasing fault throw and length. (VE 1:1).

The Figure 6.*3* represents the seismic results expected for the southeastern wall of the Waterfall Canyon, and experimenting with different sizes, from the original 100 meters in height, to having this size upscaled by five and ten times. In the seismic images presented here it is possible to observe how the hanging wall drag in all images. On the images that are upscaled, the boundary between the footwall and the hanging wall is easily discernible. However, on the true scale model, the resolution is lower, and this boundary become less visible and harder to be observed. The loss of resolution could even cause a misinterpretation of reflectors as it is possible to see on the true scale how reflectors in the Cedar Mountain Fm. Sandstone and the Tidwell Mb. are partially fused.

30 Hz, 45° Max. Illumination

Figure 6.4: Synthetic seismic analysis of the main fault area of the western wall of Courthouse Canyon. The model upscaling increases from top to bottom, the real size to ten times upscale, increasing fault throw and length. (VE 1:1).

The juxtaposition of the rocks of the Entrada Sandstones in the footwall with the Morrison formation in the hanging wall creates a visible threshold where both sides of the fault can be identified, as can be seen in Figure 6.4. However, some distortion is also generated due to this change in impedance and due to the fault dip being higher than the illumination angle, chosen in this set to be 45°, making it difficult to notice the adjacent subsidiary fault with a much lower displacement. That analysis is for the upscaled last two images of the figure, since in the true scale image, even the main fault is almost indistinguishable, and the reflectors from both the footwall and hanging wall look like they are connected or belong to the same equivalent beds.

6.3.2 Fault complexity

Other canyons in the same area expose a series of more complex networks of structures than the ones previously shown here. The Courthouse Canyon had subsidiary faults beyond the main one, with some containing an intense network of subsidiary faults. The Tusher Canyon represents a cross-section through a relay zone, with multiple faults in its interior. And the Bartlett Wash has a series of large-sized lenses in its fault area. All of these structures can impact reservoir connectivity.
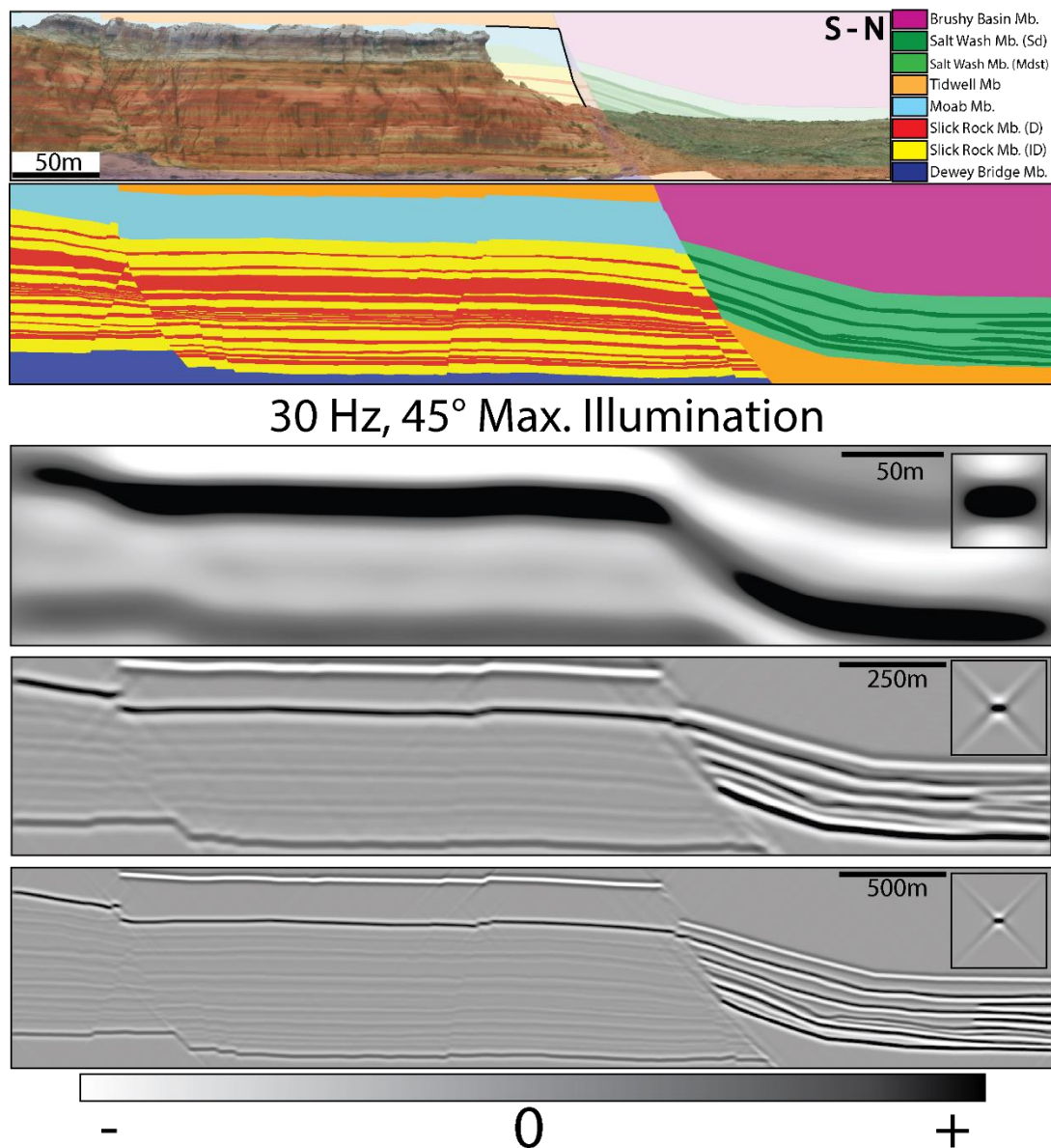
Figure 6.5: Synthetic seismic analysis of the western wall of Courthouse Canyon. The model upscaling increases from top to bottom, from the real size to ten times upscaled, increasing fault throw and length. (VE 1:1)

Figure 6.5 is an excellent example of how smaller features and deformation structures can vanish from seismic imagery when it goes under the minimum resolution. Beyond the previously mentioned main fault, not only are most subsidiary faults completely missing on the true scale image, but even the subsidiary fault with most displacement is reduced to a simple "bump" on the reflectors that could be dismissed or entirely unnoticed by someone interpreting this image. However, even though the upscaled images have a much higher resolution, many of the minor fault displacements are still a challenge to properly interpret.
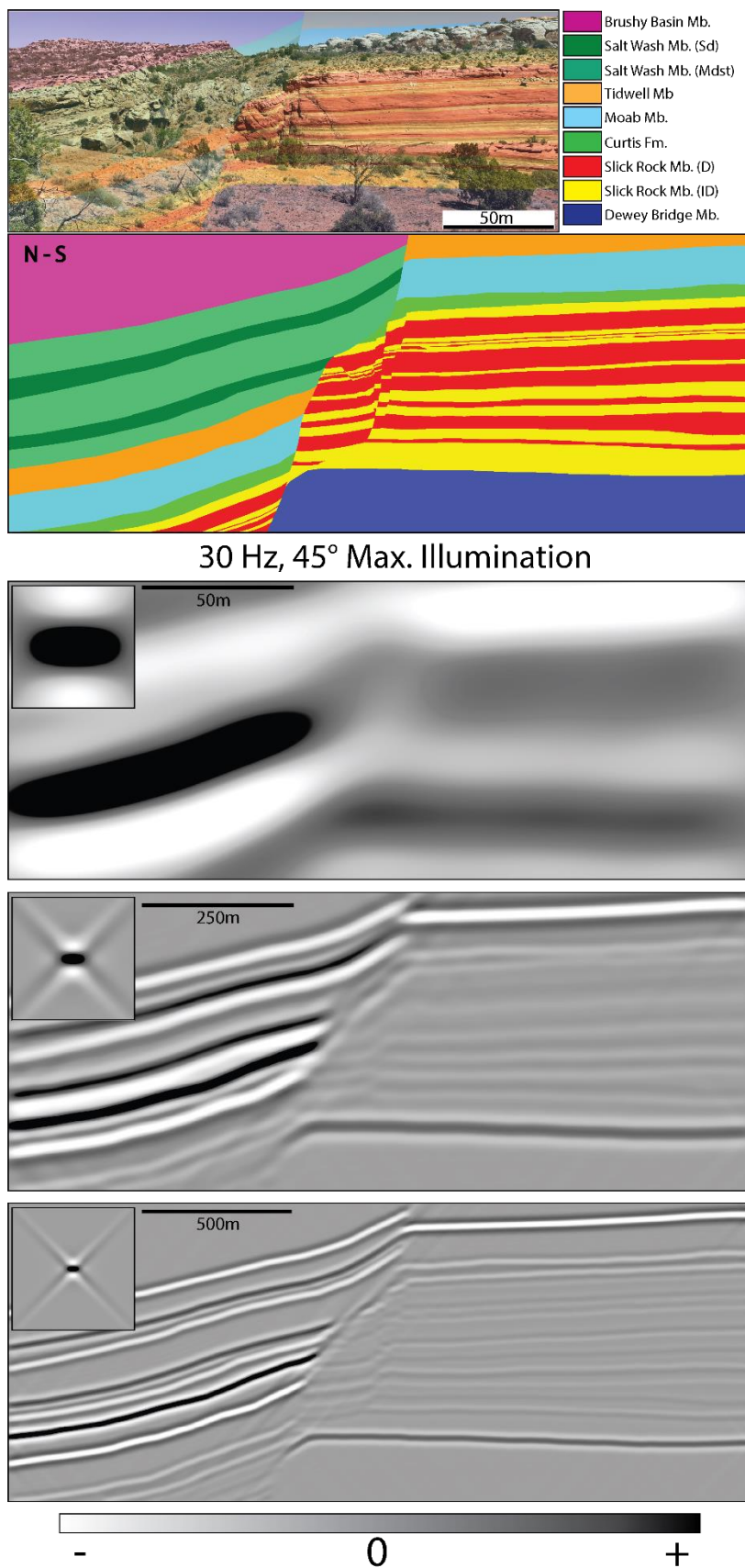
Figure 6.6: Synthetic seismic analysis of the main fault area of the eastern wall of Tusher Canyon. The model upscaling increases from top to bottom, the real size to ten times upscale, increasing fault throw and length. (VE 1:1).

The Tusher Canyon exposes a very interesting set of structures. It represents a transversal cut of a relay zone, exposing another set of fault complications internal to that zone. As expected, in Figure 6.6 these complications are seismically discernible at maximum upscaling, where these minor faults have a much higher length and displacement than the true scale model. However, at true scale, the whole structure almost disappears on the synthetic seismic image.
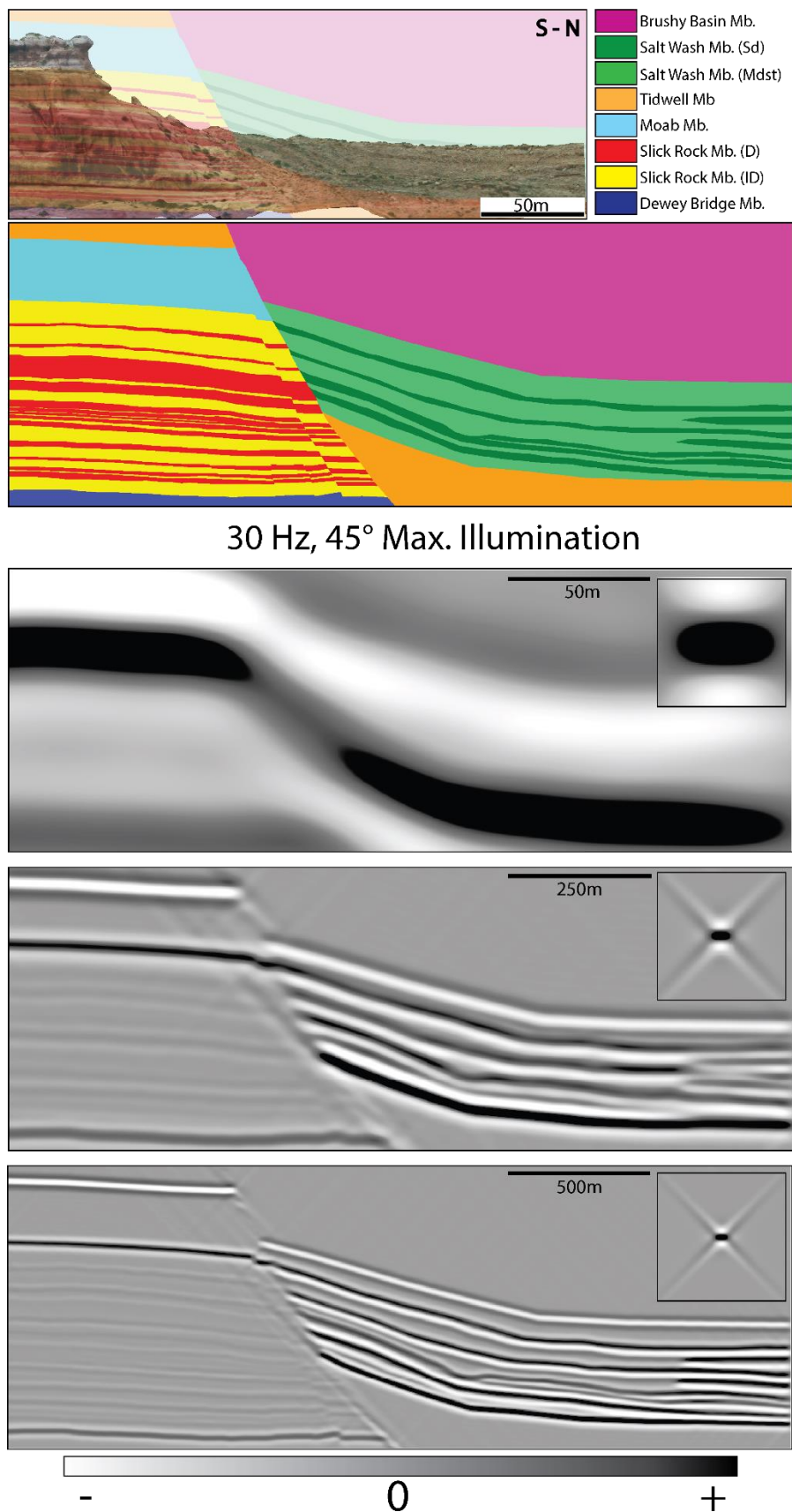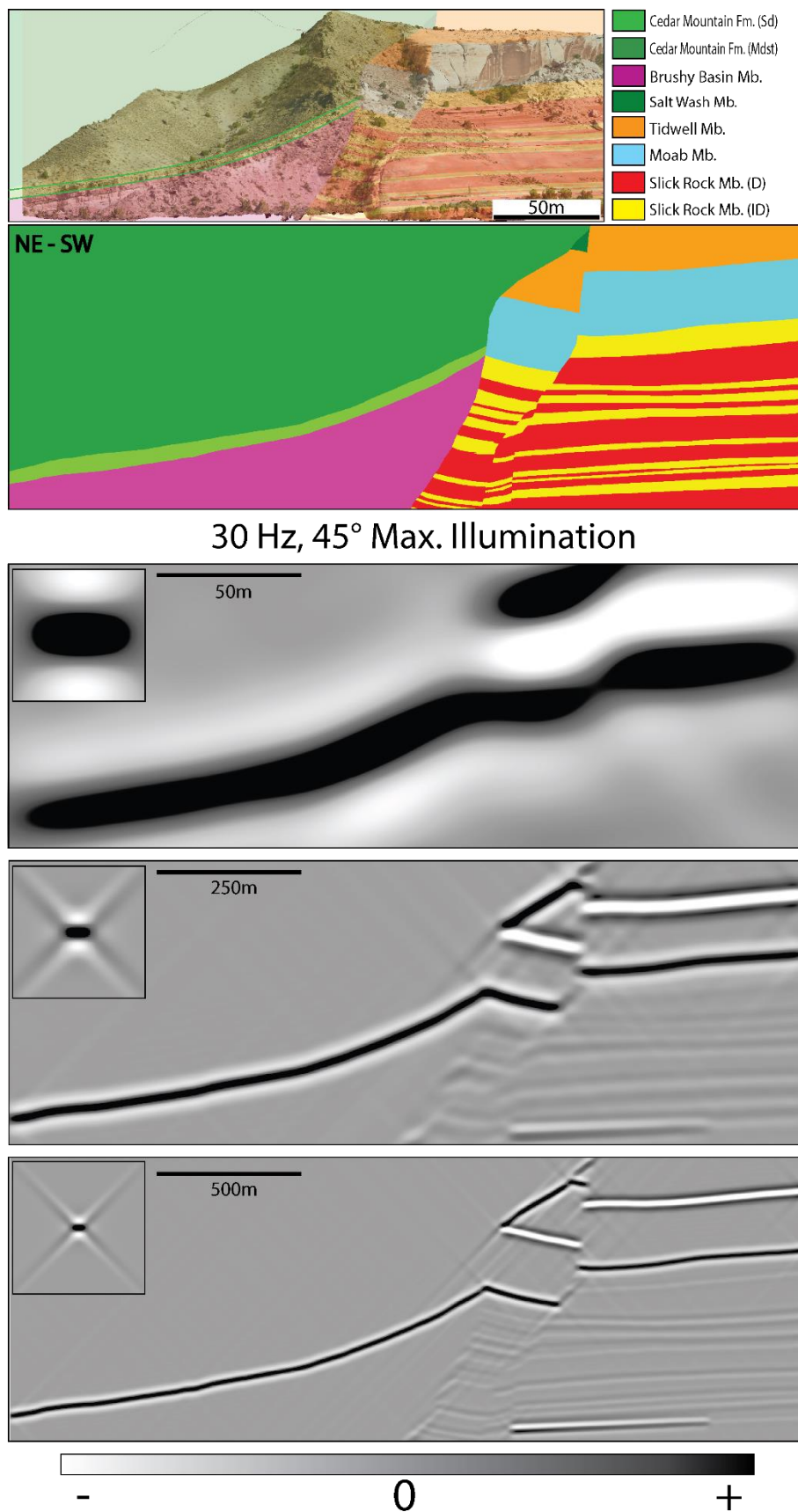
Figure 6.7: Synthetic seismic analysis of the main fault area of the southeastern wall of Bartlett Wash. The model upscaling increases from top to bottom, the real size to ten times upscale, increasing fault throw and length. (VE 1:1).

Characterised by its many large fault lenses, the Bartllet Wash wall represented in Figure 6.7 follows the same trend as the previous figures. In the maximum upscaled image, many of the structures are easy to identify, and their reflectors are easy to delineate due to their increase in size. In contrast, most details are obscured in the true scale image, with only some faint indications of a subsidiary footwall fault.

6.3.3 Sensitivity analysis

The seismic signature of subsurface structures can be affected by many different parameters, deeply affecting its resolution and detectability. Sensitivity analysis is the process where these parameters are modified to verify their influence on seismic images. In the images presented in the previous section, the same parameter values were used for all.The dominant frequency set to 30 Hz, the illumination angle to 45°, the incident angle to 0° and noise to 0%. In this section it will be discussed how varying these parameters can have an impact on the imaging, with the parameters that will be investigated in the sensitivity analysis being:

- Frequency content
- Angle of illumination
- Incident angle
- Noise

6.3.3.1 Frequency content

Frequency is a parameter that profoundly affects the resolution of a seismic image, as it defines what will be the smallest reflector that can be imaged. Five different frequency values were used for the sensitivity analysis to model the seismic images, all with a Ricker wavelet. The values are 10 Hz, 20 Hz, 30 Hz, 40 Hz and 100 Hz. The reason behind choosing these values is that the frequencies between 10 and 40 Hz represent reasonable frequencies in conventional seismic, while the higher frequencies represent high-resolution seismic images encountered in shallow structures (Reiser et al., 2012).

In Figure 6.8, a section of the Tusher Canyon east wall was used to generate a range of synthetic seismic images with different dominant frequencies for the wavelets. Since the deformation structures in the Tusher Canyon vary from large-scale faults (100 m displacement) to smaller ones surrounding the main structures, changes in frequency values would be an ideal test of the resolution intensity for these structures and its limitations. For the frequencies in the true scale models, the low resolution almost does not allow for even the main fault visualisation, except

for the high 100-Hz model, which would be equivalent to the resolution of a low-frequency image of the five-times upscaled model. For the upscaled models, the main fault is visible in all images. However, the smaller structures become visible only when applying a higher frequency.
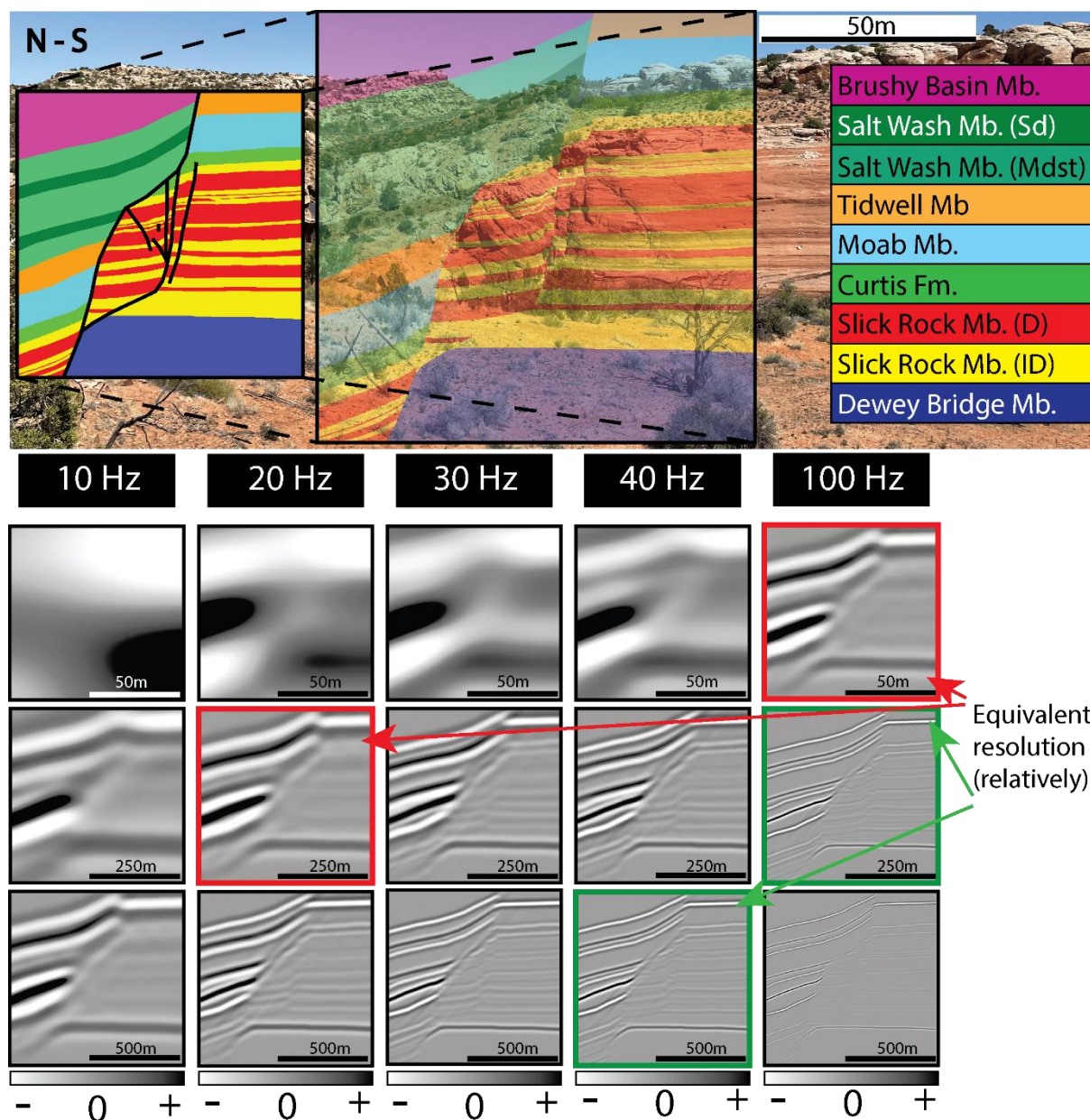
Figure 6.8: Comparison between the resolution of different synthetic seismic using different wavelet frequency values in the Tusher Canyon model. Images outlined in the same colours (except black) would have an equivalent resolution.

6.3.3.2 Angle of illumination

As explained in chapter 4, the maximum angle of the illumination vector will affect how the different reflectors will be imaged since, for them to be correctly imaged, the illumination vector must be perpendicular to the structure. This is not a problem for sub-horizontal

structures, like the stratigraphy of an undeformed basin. Still, it may deeply affect deformational structures like faults with a dip angle higher than the maximum illumination angle, thus not being imaged directly, but being detected as discontinuities and/or amplitude variations in the seismic images (Bradaric et al. 2021). In this thesis, some models were modelled with 30°, 45°, 60° and 90° maximum illumination angles. These maximum illumination angles represent realistic values (30° - 60°) (Rabbel et al., 2018), while the perfect illumination scenario (90°) is unrealistic but does help better appreciate the illumination impact on seismic images (Lecomte et al., 2016).
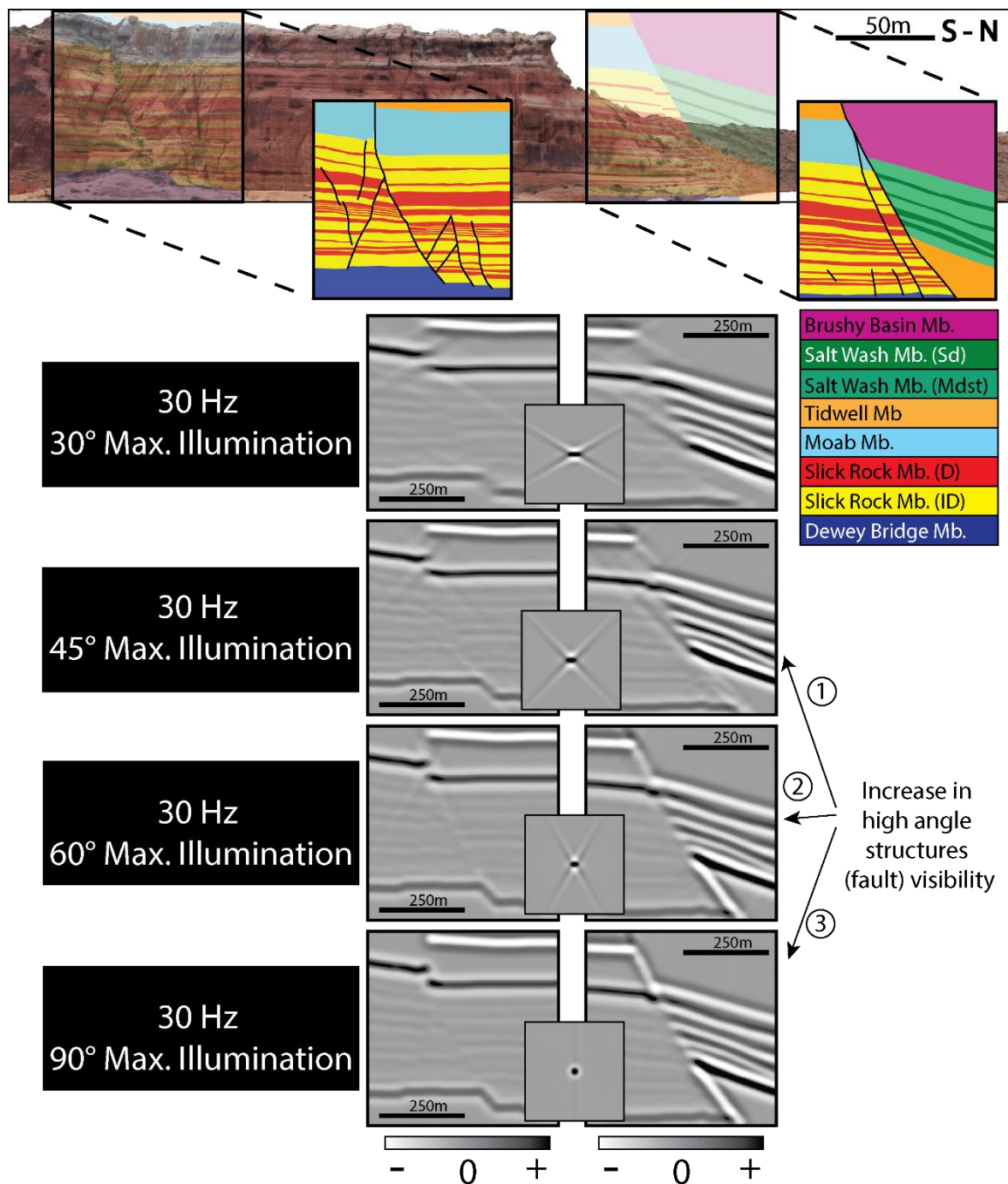
Figure 6.9: Comparison between of resolution impact of illumination maximum angle of high degree angle structures in models from the west side of the Courthouse Canyon. 1) shows an image where the fault cannot be imaged. 2) Show the moment the fault starts to be imaged, as the maximum angle is high enough to be perpendicular to the fault. 3) Shows the perfect illumination image, where all the faults are properly imaged and appear as reflectors.

As explained, any structure with an angle above the maximum illumination angle would not be imaged during the seismic data collecting process, leaving behind discontinuities or amplitudes variation. This process can be seen in Figure 6.9. The Courthouse Canyon main fault was measured as having a 72° dip angle. The impact can be seen in the synthetic seismic images

generated. For example, with an illumination maximum angle below 60°, the fault is not imaged, only identified through the displacement of the local stratigraphy. For the 60° and perfect illumination, the fault creates a proper reflector in the image. Although the average angle of the fault is higher than the 60° illumination maximum angle, the reflector is also generated probably due to a slight variation in the angle that puts it closer to the maximum angle and due to distortion in the image used to produce the geometrical model.

6.3.3.3 Incident angle

The reflectivity and seismic resolution depend on the incident angle of a seismic ray, since as it increases it may result in a shortened illumination vector span (Lecomte et al., 2016). As mentioned, the angle value of this angle can affect the resolution and thus impact the level of geological details which can be observed on a seismic image. The seismic images in this thesis were modelled with the incident angle of 0°, 20° and 40°, as these angles stay below the range where the critical angles for the boundaries trying to simulate real seismic, where these high angles would be muted before migration.

As shown in **Error! Reference source not found.**, the incident angle's effect on reflectivity is related to the reflection coefficient, with different boundaries having different behaviours as the angle is increased or decreased. Depending on the velocity and density parameters of the above and below beds, different boundaries are affected differently, with the coefficient raising or lowering as the incident angle increases.
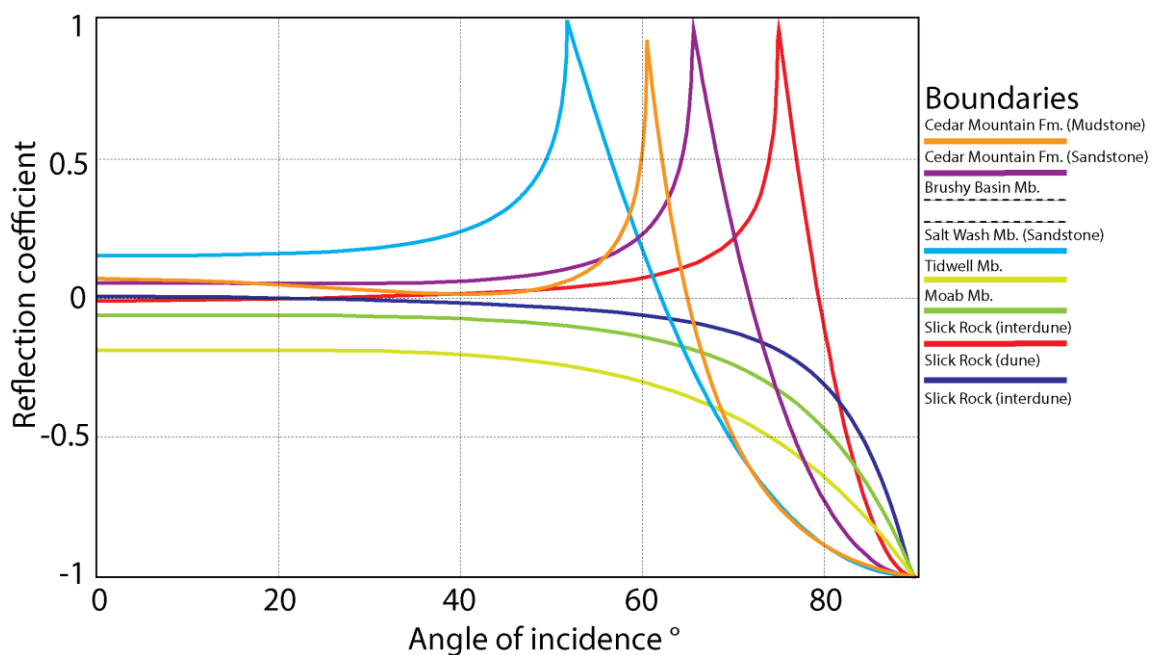
Figure 6.10: All layers boundaries from the Bartlett Wash southeastern side model and their differences in reflection coefficient with the increase in the angle of incidence.

In the analysis done in Figure *6.11* to observe the impact on resolution caused by changes in the incident angle due to the different reflection coefficient behaviors for each of the boundaries, differently oriented reflectors had their resolution impacted differently by this angle changes. There is an overall loss of detail, both horizontally and vertically, as the incident angle is increased. The horizontal reflectors seem to get more laterally smeared, and the vertical ones more smoothed. This had little impact in interpreting the upscaled models, but it would impact the true scale mode, as it homogenizes the primary reflector and disappears with the fault.

Another interesting phenomenon observed was the impact in the boundaries between the dune and interdune beds of the Slick Rock Mb., as they initially show a loss of resolution when the incident angle is increased to 20°, with the reflectors almost disappearing, and return with their polarities reverse when the angle is increased further to 40°. On further observation, this happens due to a change of polarity of the reflectors in the beds of this unit, and the cause of this becomes evident as the angle of incidence vs reflection coefficient graph in Figure *6.12* shows that both boundaries start with positive and negative reflection coefficient values, that reach a value of zero near the 20° value, and then transition to an opposite value further on. This becomes important as the image resulting from the sum of the incident angle values is analysed, having a very low resolution compared to other values, as, in this scenario, the sum of the angles partially nullifies the reflection coefficient.

Figure 6.11: Comparison of the impact on the resolution of different structures caused by changes in the incident angle in the southeastern side of the Bartlett Wash model.
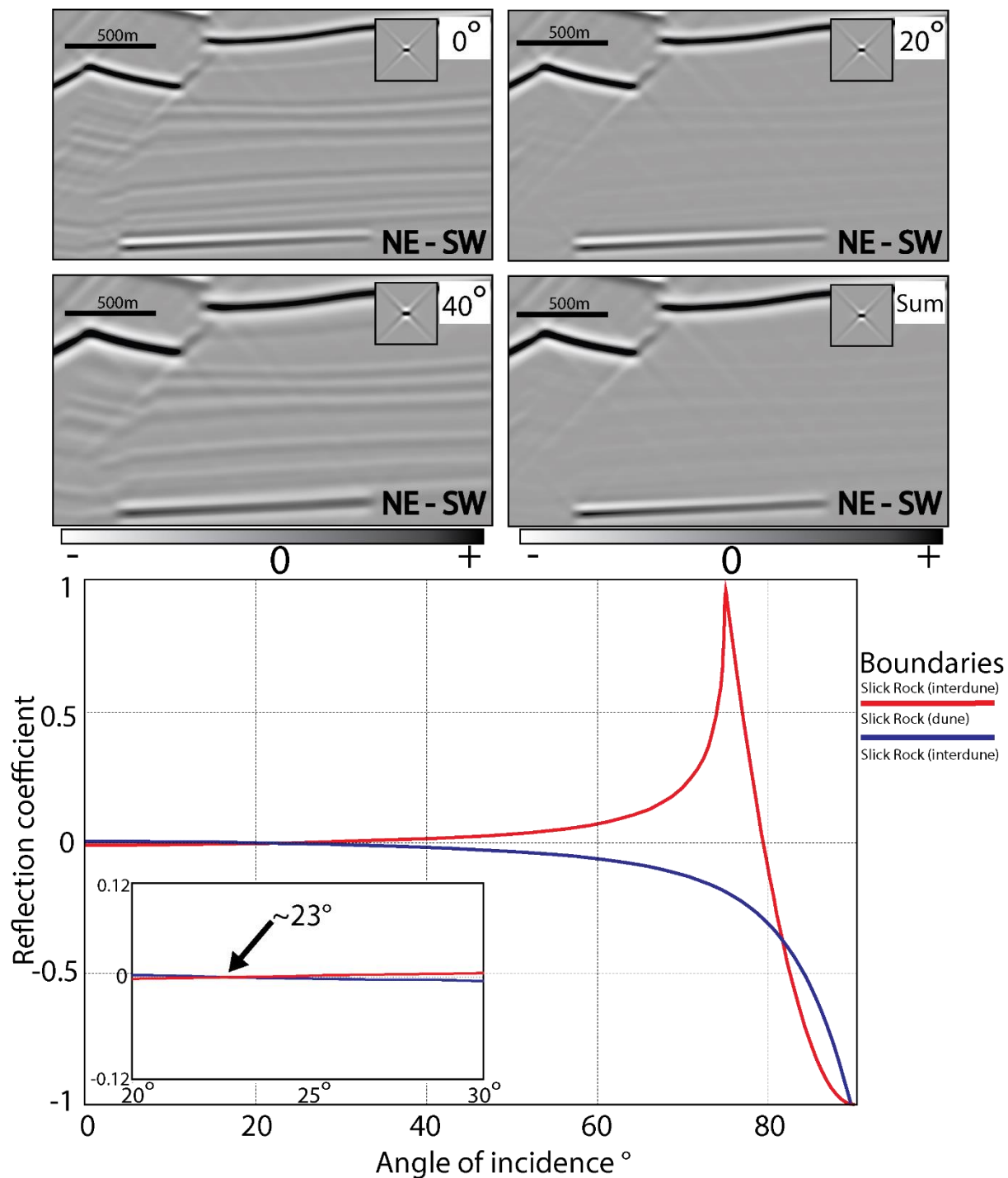
Figure 6.12: In depth analysis of the changes in reflectivity of the Slick Rock Mb. of the Entrada Sandstone as the incident angle is changed. The polarity for the imaged beds are reversed when the incident angle is around 23°, with a brief moment where the reflection coefficient, during its reversion, has a value of zero.

6.3.3.4 Noise

The final step to analyse the impacts of the many parameters that may affect seismic images is to study the effect of noise. Following the steps of Lubrano-Lavadera et al. (2018), a PSDM noise model was generated by convolving a white random noise grid with the analytical PSF to

simulate the noise found in real seismic. These "Noise Models" were superimposed on the synthetic seismic models, following a range of noise amplitude (the signal-to-noise ratio) from 0% to 100% in steps of 25%.

In the noise analysis of the synthetic seismic image from the Bartlett Wash northwest side (Figure 6.13), the low-intensity reflectors, like the ones between the different beds of the Slick Rock Mb. disappear as soon as just as low as 25% of noise intensity is applied, leaving behind just the stronger reflectors. However, even these strong reflectors become harder to observe as the noise intensity increases, with their visibility significantly blurred at 100% noise intensity.
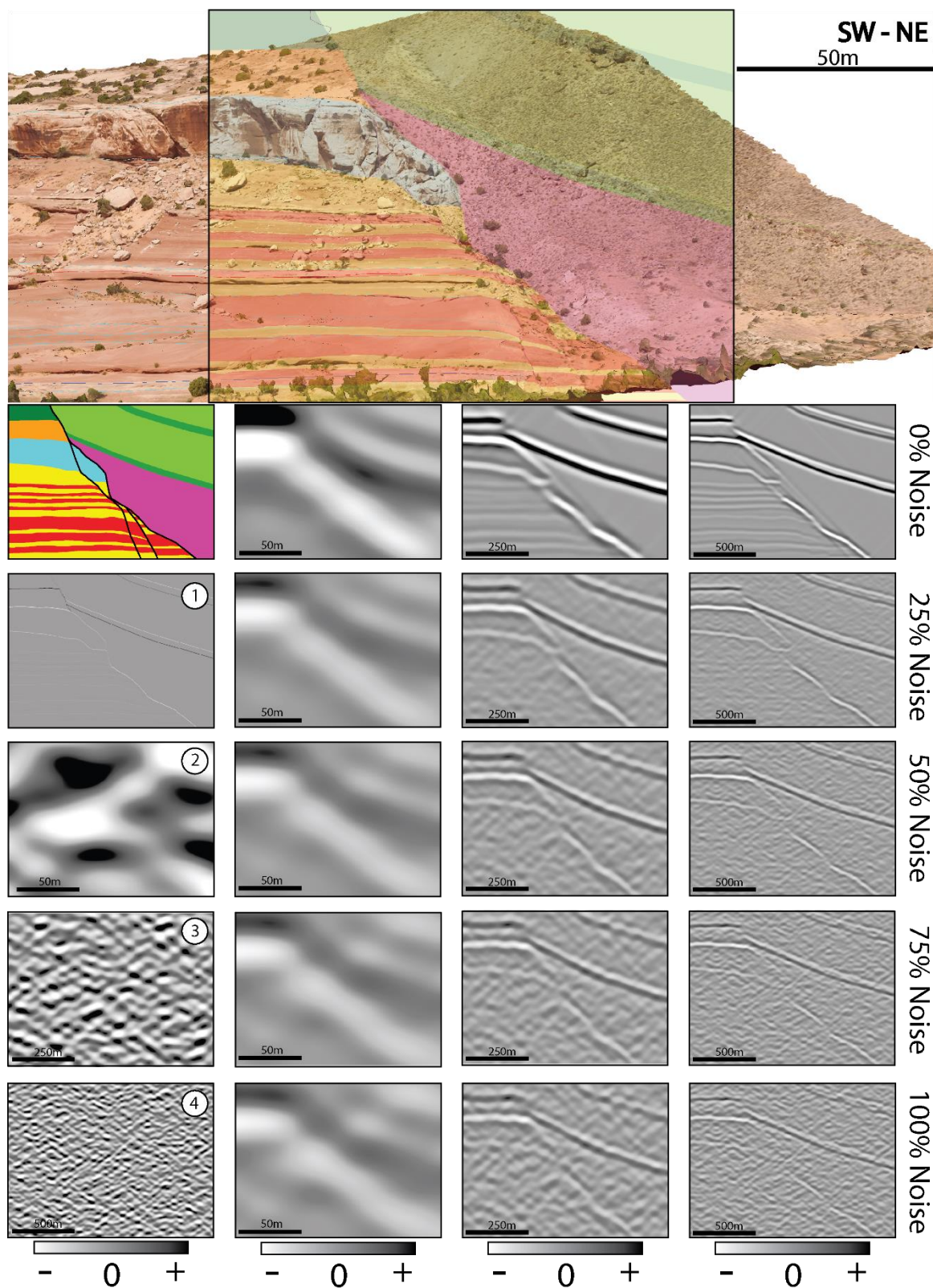
Figure 6.13: Comparison of the impact on resolution of different structures caused by changes in the noise intensity in the northwestern side of the Bartlett Wash model. All images have 30 HZ as dominant frequency and 45° illumination. 1) shows the reflectivity model .2), 3) and 4) show the seismic noise created and then added to each modelling case.

7. Discussion

This thesis has aimed at increasing our understanding of fault and fault zone complexities and how these structures are captured in seismic data based on the production of synthetic seismic images of real field examples. First, a proper comparison between previous works on synthetic seismic structural elements and the elements and methodology used in this thesis will be made (section 8.1), followed by an analysis of the results obtained through applying a normal fault system to synthetic seismic (section 8.2). After that, the sensitivity analysis results will be addressed (section 8.3). Lastly, a comparison between the synthetic seismic and the real seismic data from the North Sea rift will be made, addressing all the comparable structures found in both images (section 8.4). Seismic modelling results are also presented in a PowerPoint file for better visualization of results, including images not presented here (Seismic modelling results).

7.1 Comparison to previous work

As seismic modelling methods and tools have become better developed, several works have been performed that study how features from both the geology and seismic parameters can influence the production of real seismic data (e.g., Jackson et al. 2014; Faleide et al. 2021,2022; Flæte 2022; and Volatili et al. 2022). In the multitude of works dealing with synthetic seismic, a few tackles the same object of study as this thesis of how fault interpretation can be affected by the seismic resolution and which parameters cause the increase or loss of detail in these images. One the article by Jackson et al. (2014), where generic models of normal faulting were produced using 1D convolution methods. As previously mentioned, Lecomte et al. (2015, 2016) point out that this method generates models that do not address lateral resolution issues- and limited-illumination effects. Though the 1D convolution method may help evaluate vertical resolution impacts on seismic images, the simplicity of this modelling technique may lead to errors that were avoided by using the PSF-based 2(3)D convolution method used in this thesis.

As the technology and the methodology for seismic modelling and the construction of synthetic seismic images became more advanced, more works were build on these new tools and knowledge, including more recent works that use the same PSF-based 2(3)D method for faults, as the one used in this thesis (Faleide et al. 2021, 2022; Flæte 2022; and Volatili et al. 2022). One of the most important differences between these works and this thesis is the basis used for the seismic modelling, both in the sense of the geometrical and elastic parameters used. For

Flæte (2022), generic models were constructed to serve as the basis for the modelling, allowing for the production of target structures to be analysed. This kind of subject allows for a detailed study of specific target structures, but isolated, without a more complex background found in modelling based on real examples. In this same work, other method used was the production of geometrical models based in plaster models, allowing for a seismic modelling process that would be more analogue to the structures found in outcrops or in subsurface. Another subject explored in Faleide et al. (2021, 2022) was the use of interpretations of real seismic, allowing for a more dynamic and complex model that the final results can later be compared with the original seismic. This process, although beneficial to check how close the synthetic seismic results are to the real ones, will produce models based on the interpretations that suffer from a limited resolution.

The final of the three possible subjects for seismic modelling that will be discussed here is also the one used in this thesis. The modelling based on real outcrops from other authors follows a similar approach but differs in two aspects: The outcrop and the elastic parameters used as a basis. In the recent work by Volatili et al. (2022), the outcrop used were platforms carbonates expositions in a basin-bound normal fault scenario. Also, Dimmen et al. (2022) studied faults in carbonates. This thesis chose a different scenario, focusing focused on an extensional fault system with the elastic parameters for siliciclastic units to yield different seismic modelling results.

7.2 A normal fault system under seismic modelling

In this study, extensive seismic modelling of the Moab Fault splay in Utah was made through a series of 2D synthetic seismic images based on geometrical models from the canyons that cross the fault in multiple places. This rather unique sequence of canyon-based geologic section and modelled seismic images allows us to study lateral changes in fault zone geometry and anatomy and how this can appear in seismic data. The sequence of images produced is shown in the sequence in Figure 7.*1* and Figure 7.*2*. As mentioned in previous studies, the number of deformation structures found in the Moab Fault Splays is shown to increase near the abutting of the Moab and the Courthouse Fault. However, this can be seen only in the upscaled models and in the higher resolution images, as the subsidiary deformation structures have a much lower displacement and thus are invisible or barely visible in the seismic. In the true scale images, as can be seen in Figure 7.*2*, even the main fault is sometimes hard to observe, since some of the

reflectors from the footwall and hanging wall, which are of close amplitude, get fused and could be easily misinterpreted as a lateral variation in stratigraphic dip angle or as a fold. And, although the fault system evolution can be seen with higher resolution, like in Figure 7.*1*, when real size images with what would be considered a common frequency in seismic imagery (30 Hz), it becomes much harder to observe the evolution, as most of the smaller structures are now under the resolution limit.
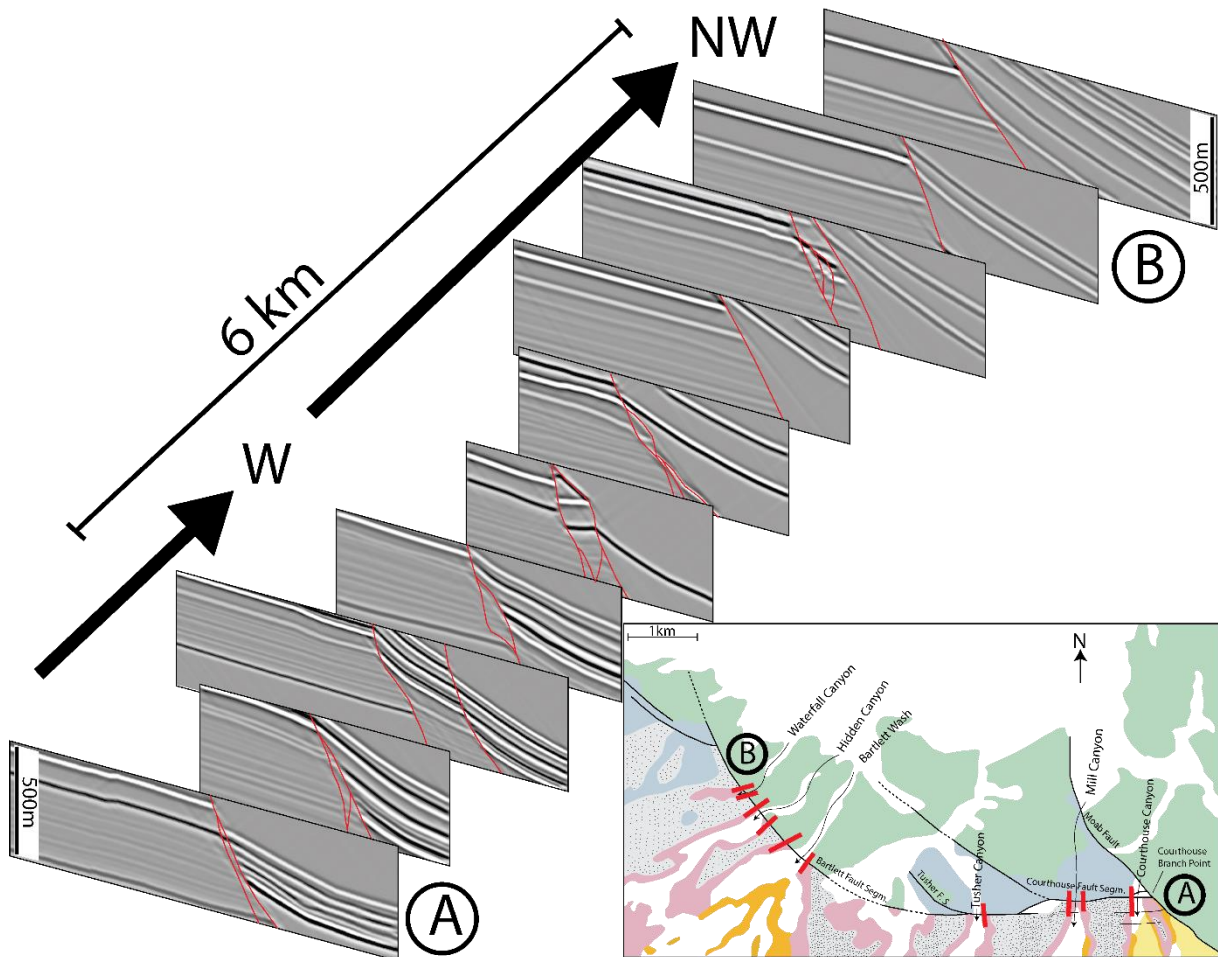
Figure 7.1: Seismic modelling panels produced from the outcrops in Utah put in order from the eastern to the westernmost. The images here represent the outcrops upscaled five times, with 500 meters high, 30 Hz dominant frequency and 45 deg illumination. Red lines in the seismic images represent the placement for the faults based on the original geometrical model. Regional map modified from Berg and Skar (2005).
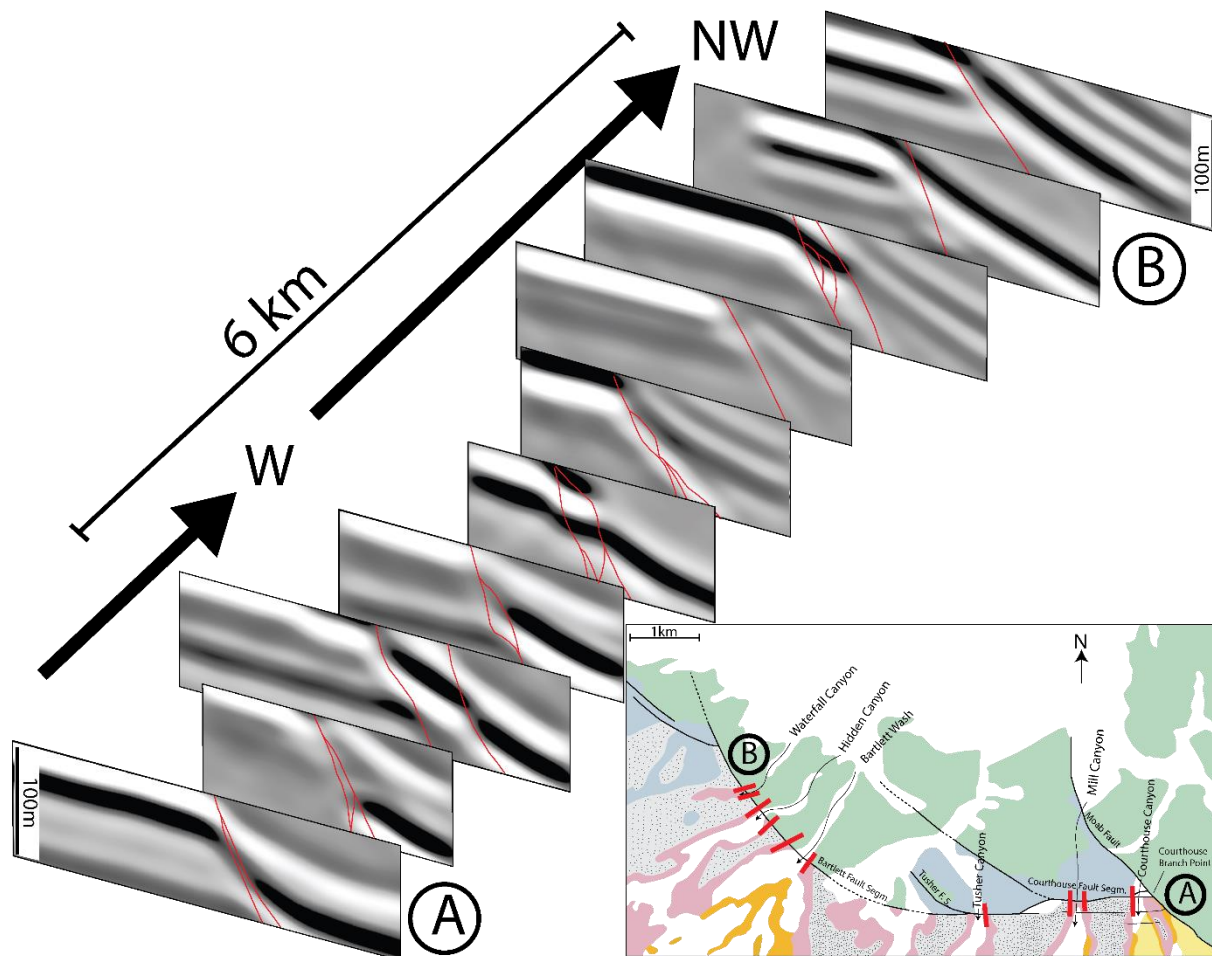
Figure 7.2: Seismic modelling panels produced from the outcrops in Utah put in order from the eastern to the westernmost. The images here represent the real size outcrops, with 100 meters high, 30 Hz dominant frequency and 45 deg illumination. Red lines in the seismic images represent the placement for the faults based on the original geometrical model. Regional map modified from Berg and Skar (2005).

Another visible aspect of the fault system is the change in offset along the strike, which starts around 80 meters near the abutting of faults and increases as we move along the fault. Unfortunately, due to a large gap between the Tusher Canyon and the Bartlett Wash (more than 2.5 km, as compared to the average 1km distance between the other canyons), there is a jump in the otherwise fairly regular spacing between the seismic images produced from these canyons, breaking the constant increase in the offset.

Finally, these synthetic seismic images allow us to observe and understand the evolution of fault structures and features as we move along strike. This applies specifically to the Moab Fault system and similar structures in this part of the Colorado Plateau, but can also be applied to other normal fault systems in siliciclastic sediments.

7.3 Fault structures under varying geophysical parameters

The sensitivity analysis done through the many models of outcrops in the Moab Fault Splay area affected how these structures were imaged seismically. Some parameters changed throughout the study had a more major or minor effect concerning how much geological detail was lost during the imaging. In the following part, the results obtained through the variety of imaging parameters and how they affected the image resolution will be discussed in the following sub-sections.

7.3.1 Effects of upscaling

The upscaling of the models has a profound impact on the seismic resolution, as, all its stratigraphic and structural features (unit thickness, fault displacement, etc.) are upscaled. As explained in Chapter 4, the produced seismic image has a minimum object size that can be identified, depending also on other factors such as the frequency. This change of scale in seismic models has already been done in the past in different styles outcrops analogues: from generic or plaster models to existing outcrops (Lindanger et al., 2004; Andersen, 2014; Jackson et al., 2014; Rabbel et al., 2018). Therefore, the impact of model upscaling can be seen as the resolution of all units and faults is increased as the model is upscaled.

For the true scale model, large displacement faults (>50 m) could still be seen in most frequencies (10-100 Hz). In comparison, low displacement faults (<10 m) were barely visible or completely invisible except for very high frequency levels (close to 100 Hz). As expected, this low resolution became less present in the upscaled models since, as mentioned before, the size of all structures is increased in the process, and they start to exceed the minimum resolution level. On the images that were upscaled ten times, even smaller subsidiary faults began to be properly imaged in the image, as simples five meters displacement faults were transformed into 50 m displacement faults.

7.3.2 Effects of dominant frequency

As mentioned in the previous sub-section, the variation in the dominant frequency also changes the minimum size that an object must have to be imaged in seismic. The wavelets used in this thesis were the Ricker wavelet format, which has a zero-phase symmetrical shape, making it often used in seismic modelling (Jensen et al., 2021; Lecomte et al., 2016; Lindanger et al., 2004). This, however, does not represent the same behaviour as the wavelets that can be extracted from real seismic data, as they tend to be asymmetrical (Wang, 2015). As the software used to produce the seismic images used in this thesis does not allow modelling with non-zero-

phase wavelets, the modelling done in this thesis was made through the previously mentioned symmetrical Ricker wavelets.

With the 10 Hz increase for each step from 10 to 40 Hz done in this thesis, it is easy to observe how the resolution is improved between each step. In the same manner, as the upscaling of the models, the low-frequency images only visualize the main fault. For the true scale models, the resolution is so low for the 10, and 20 Hz frequencies that the images produced resolve very little of both the stratigraphy and the fault. For frequencies of 30 and 40 Hz, the increase in resolution is enough to visualise minor faults in upscaled models and major faults in the true scale one. The 100 Hz frequency, representing what would be the resolution in high-frequency seismic, allows for enough resolution for these images so they can be compared to similar resolution images in upscaled versions of themselves made in lower frequencies.

7.3.3 Effects of illumination angle

As the illumination angle defines which structure will be imaged or not in the seismic, through the process mentioned in Chapter 4 where only reflectors that are perpendicular to the illumination ray will be imaged, a model based on a normal fault system with faults with an average dip angle around 60° was heavily impacted by this parameter. For illumination angles found in regular seismic (30°-45°), the faults, as expected, did not produce reflectors that could make their interpretation easier and were only visible through the contrast between the reflectors produced by the units in the hanging and footwall. If a fault were to cross an area where units on both sides were homogeneous and had little difference in their elastic parameters, it would make it barely visible to completely unidentifiable depending on the distortions found in that seismic. A few of the faults produced reflectors within this range of illumination, but it was due to these sections having a lower angle, due to changes in the fault network, and making them imageable.

With an illumination angle of 60° and 90° (perfect illumination), faults in the models began to produce proper reflectors in the seismic image. However, for faults with small displacement, where most of the units are still laterally juxtaposed on both sides of the faults, no reflector is generated, due to a lack in changes of the elastic parameters rather than due to problems with the illumination angle. The illumination angle can be considered one of the most important parameters in fault detection in seismic images; however, due to limitations in wide this angle can be in real seismic data, little can be done when analysing areas dominated by normal faults to avoid this problem.

7.3.4 Effects of incident angle

As the incident angle of an incoming seismic wave affects the reflectivity model and the PSF, the increase and decrease in this angle will impact the resulting seismic image. In this thesis, the deformation structures analysed suffered an overall reduction in resolution as the incident angle was increased ($0°$, $20°$, $40°$), becoming harder to define the limits of larger faults and distinguish the smaller ones. As the reflectivity contrast between some layers, such as the boundaries between the Slick Rock and Moab Mb., changes with the increase of the incident angle, it becomes harder to detect the full extent of the faulting, with this having a higher impact on the true scale models, with the little amount of detail that existed in these images that could be associated faulting, disappearing under the increase of the incident angle.

Although the increase in angle decreased fault resolution in most of the images, an exception was found that is presented in **Error! Reference source not found.**. Due to the member having two different lithologies (dune and interdune) intercalating each other, and their boundaries behaviour in the incident angle vs reflection coefficient graph, their increase in angle from $0°$ to $20°$ did decrease the resolution, but the increase from $20°$ to $40°$ did the opposite and, due to the inversion in polarity of the reflectors, had an increase in resolution, allowing for the faults to be visible again. The resolution at this higher angle is not as high as when the incident angle was set to $0°$, but definitively higher than when it was set to $20°$. Although lower incident angles have the highest resolution, in real seismic, due to the seismic exploration, the angle may be diverted as the depth is increased, generating a higher incident angle (Eide et al., 2018). Understanding the behaviour of each boundary as the incident angle change is also essential, as they may cause pitfalls where one could generate low-resolution images in certain angles, as mentioned previously.

7.3.5 Influence of Noise

Due to how the PSF-based convolution method produces an ideal PSDM synthetic seismic image with no noise, levels of random noise were added to it (25%, 50%, 75% and 100%) trying to produce more realistic seismic images and to evaluate how these different levels would impact the detectability of faults and the stratigraphy in the subsurface as it would in real seismic (Simm and Bacon, 2014). As expected, the addition of noise decreased the visibility of structures in the seismic images. As the noise intensity was increased, only the reflectors, like the interface between Slick Rock and Moab Mb. or the interface between Moab and Tidwell Mb., were still distinguishable in the image, with weak reflectors, like the one from the different layers from the Slick Rock Mb., almost being erased from the image as soon as 25% of noise

was applied. Smaller faults and other deformational structures are challenging image properly, even in a clean image without or with very little noise. With the presence of noise, these structures can be rendered entirely invisible to whoever is interpreting the seismic image.

7.3.6 Summary of geophysical paraments effect

The sensitivity analysis result shows that the imaging of faults and fault zone in seismic images can be impacted by many different parameters of the seismic modelling process. Some of these parameters may have a more pronounced effect on the resolution than others, such as the dominant frequency, that its increase will make smaller faults to become visible, or illumination, that will have an important impact in imaging faults as proper reflectors. However, none of the parameters studied here should be ignored if we are to understand the limits and pitfalls. The results presented in this study show how complex the detection of faults and faults zone in seismic images can be and how challenging it would be to set a resolution minimum for these structures, as multiple parameters affect its visibility.

7.4 Comparison of synthetic and real seismic data.

Much of the work done in this thesis related to synthetic seismic modelling was made with the final goal of using it as a basis to improve the understanding and interpretation of fault systems in seismic images collected around the world. Due to all previous works presented here concerning the fault theoretical background (Kearey, 1993; Caine et al., 1996; Maerten et al., 2002; Bailey et al., 2002; Grasemann et al., 2005; Soliva et al., 2006; Lindanger et al., 2007; Braathen et al., 2009; Peacock et al., 2016; Fossen et al. 2020; Gent & Urai, 2020) and the works that used synthetic seismic to simulate real seismic imagery(Jackson et al., 2014; Faleide et al. 2021, 2022; Flæte 2022; and Volatili et al. 2022), it is beyond doubt that the seismic images presented here are to be used to predict behaviours that could also be found in the North Sea seismic images. During the comparison between the images produced and collected, some structures and characteristics were noticed that further increase the confidence that the synthetic seismic can serve as an analogue or could push forward our understanding of how certain structures may be imaged.

One of the first phenomena in the seismic modelling that was noticed to have a similarity with the images obtained from the North Sea was the effects caused by small displacement faults. Unlike faults with higher displacement, which cause enough displacement to also create a similar impact on the reflector, these smaller faults, as can be seen in Figure 7.*3*, can generate distortion, appearing as "bumps" or small apparent monoclines. For a complex normal fault

system that contain a series of smaller subsidiary faults, knowing where to look for them may be of great importance for the constructions of models that try to be as close as possible to reality. As real seismic can be affected by many forms of distortions and effects that may generate shapes similar to the aforementioned "bumps", it is necessary caution before using them as signs of small displacement faults under or close to the seismic resolution.
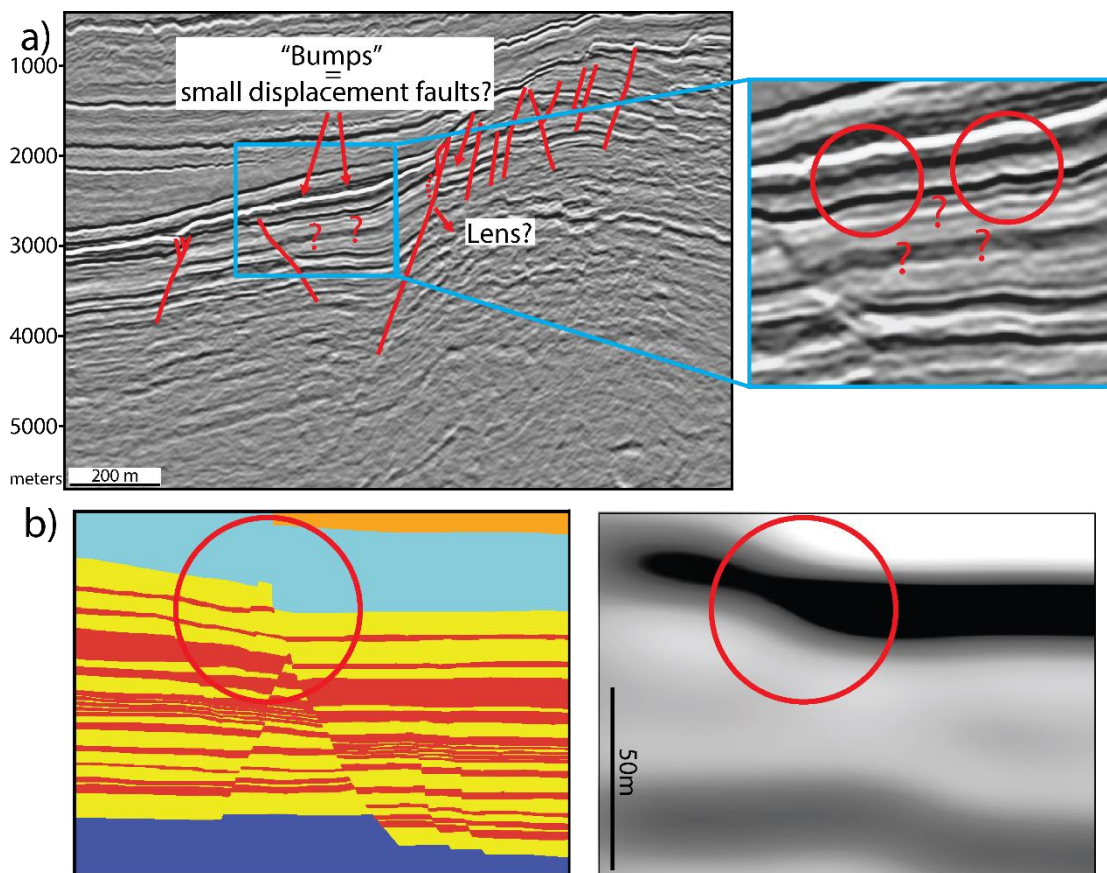
Figure 7.3: As the resolution is limited, some small displacement faults may appear in seismic imagery as irregularities in the reflectors. a) A set of normal faults from real seismic containing small irregularities ("bumps") that indicate locations of small displacement faults. b) Results from seismic modelling, with true scale model, 30 Hz dominant frequency and 45 deg angle illumination, where small displacement faults (<10 m) can be imaged as simple irregularities in the seismic.

As these distortions in the reflectors may not be definite evidence of the presence of faults, it is possible to take advantage of how their displacement changes along strike as a form to verify the existence of the structure or if it would be just a simple distortion. In Figure 7.4, an area of the study in Utah, with a different level of displacement, is shown in comparison to two different real seismic images. Both images for the North Sea area show the same fault but moving along strike. As predicted, although the topmost of the real seismic images (Figure 7.4b) shows one of the mentioned distortions that cannot be safely defined as a fault, as displacement increases along strike, the fault becomes visible, even if barely. Because even small faults can behave as

barriers or conduits for fluid flow, using this new knowledge on how to identify the structures that can hint at the location of subseismic faults and how to verify them could have a significant impact on reservoir modelling and fault prediction.

Geometrical seismic   Synthetic seismic   Real seismic
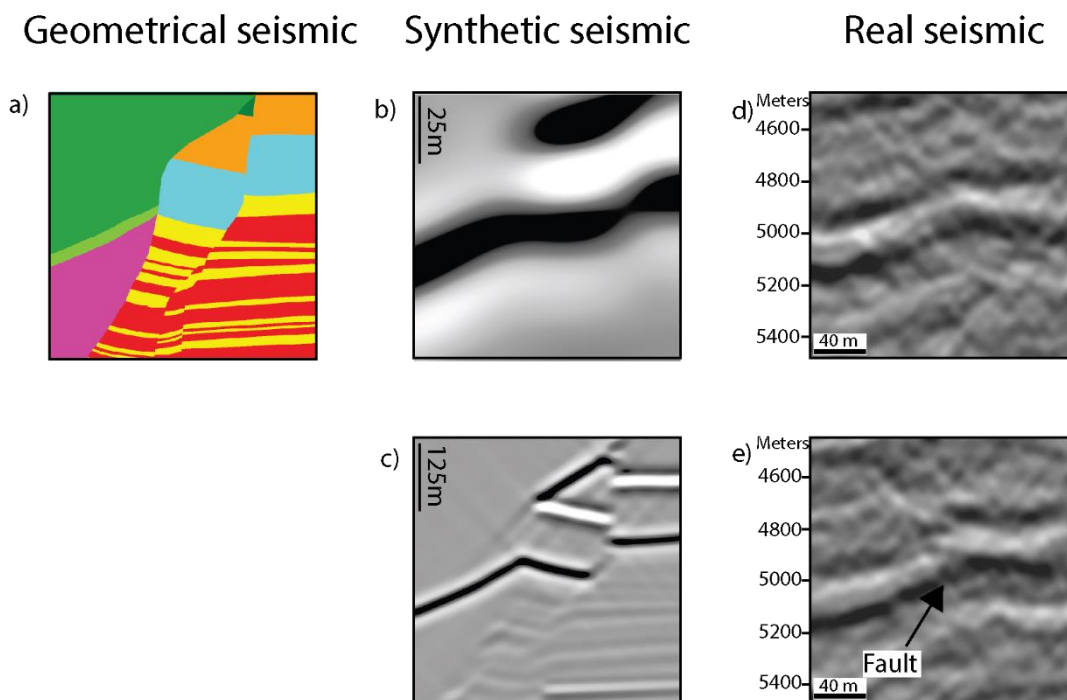
Figure 7.4: Comparison between synthetic and real seismic to show how small displacement faults may appear as simple irregularities in low-resolution seismic. a) Bartlett Wash northwestern wall geometrical model. b) Seismic modelling result for the geometrical model under 30 Hz and a total height of 100 m. c) Seismic modelling result for the geometrical model under 30 Hz, 45 deg illumination and a total height of 500 m. d) Real seismic image reflector showing an irregularity ("bump"). e) Same area as the previous image but moving along strike. A probable increase in displacement made the fault visible.

In Figure 7.5 further illustrates difficult is to interpret small scale faults and how moving along-strike mapping can help to identify these structures. The models produced based on the Courthouse section proved themselves very helpful in this discussion, as they possesses two sets of subsidiary faults, with enough distance from the main fault that interference was avoided. When upscaled by five times and with a dominant frequency of 30 Hz, the model represents the scenario of one fault barely above and another barely below resolution. Although these are not the same faults, it shows how just a few meters of difference in displacement can control whether or not a fault will be imaged. This can be compared with the real seismic images extracted from the North Sea, since the proper appearance and posterior disappearance of the fault can be attributed to the change of displacement along strike. This can be used to identify these smaller faults, but it would still be a challenge to pinpoint how far the fault would continue

sideways. For that we need to use empirical relationship between displacement and length (e.g., Fossen, 2020).
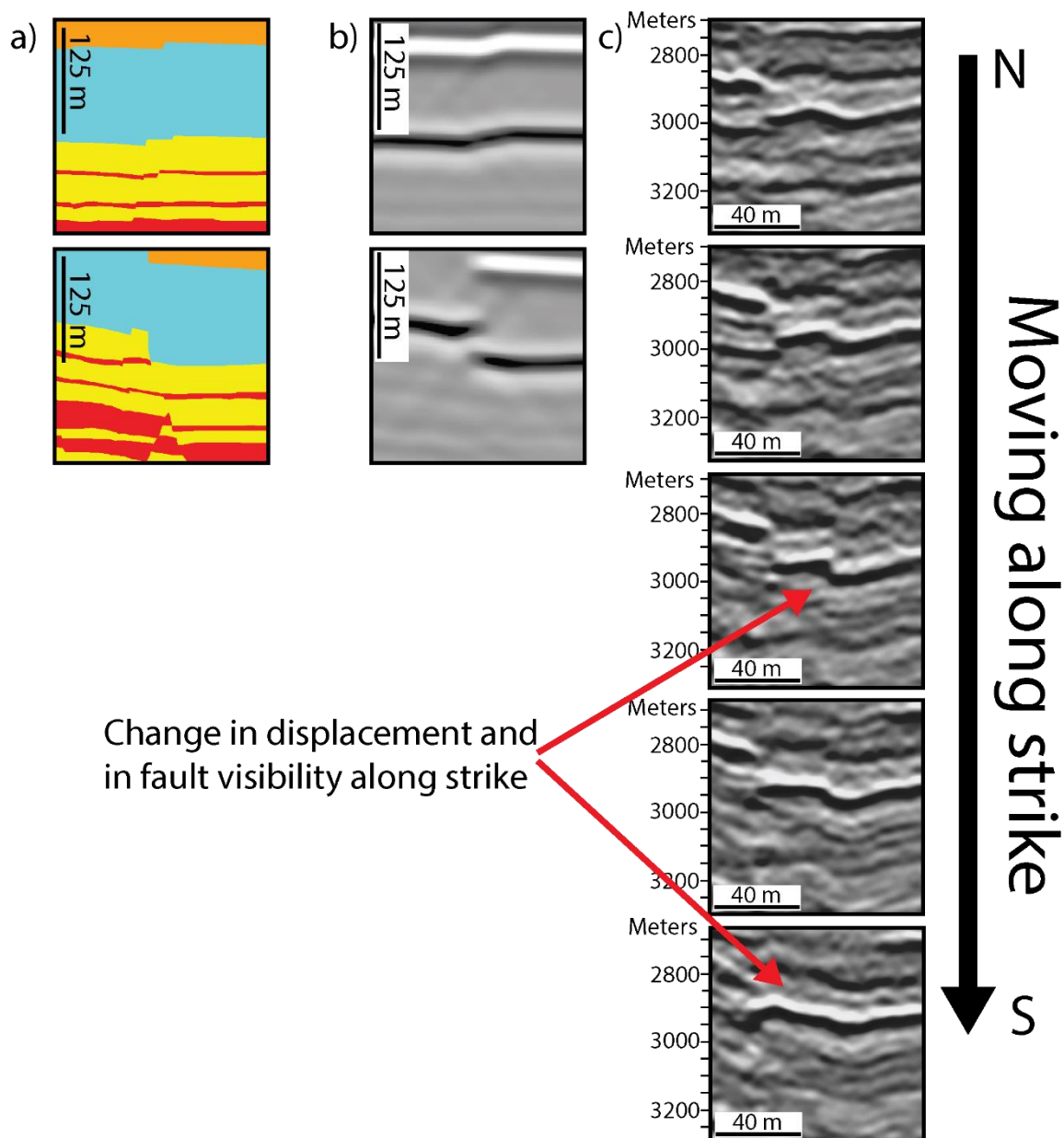
Figure 7.5: Analisys of the visibility of small displacement faults in the synthetic and real seismic. a) Geometrical models of subsidiary faults in the Courthouse Canyon outcrop. b) Seismic modelling results with a five times upscaled model, 30 Hz dominant frequency and 45 deg angle illumination of the geometrical models. c) Real seismic images from the North Sea with a small displacement fault with a change in visibility as the displacement changes as the image is moved along strike.

Another behaviour noted in the synthetic images is how challenging it is to image certain structures that run along the fault. In Figure 7.6, images from both the real and the synthetic

seismic present structures, fault lenses in the synthetic and a distorted wedge between the fault walls in the real seismic, which can be a challenge for a seismic interpretation. Based on the analysis of the various parameters that could affect the resolution, it is possible to point out the causes of this difficulty in terms of non-optimal values for dominant frequency, incident angle and illumination angle, with the latter being one of the most relevant for normal fault systems like the ones analysed here. The interpreter may not have any influence on the parameter values used in the seismic processing, and, for normal faults, rarely the illumination angle would have a high enough angle to properly image them. It becomes necessary for the interpreter to exercise extra caution when interpreting areas around fault zones, as many structures may easily go unnoticed.
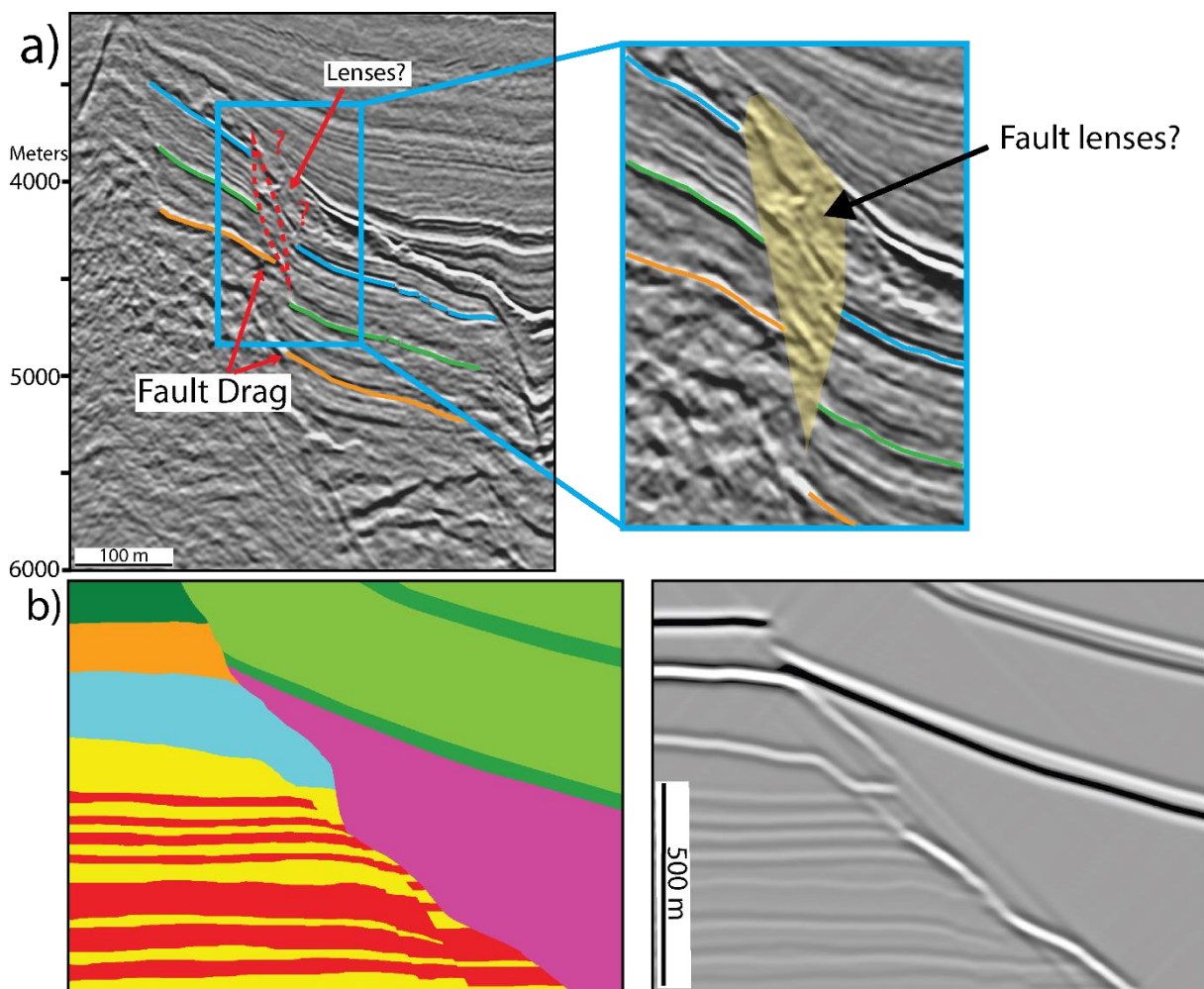
Figure 7.6: Comparison between a normal fault with an extensive fault core with possible fault lenses with the results from synthetic seismic showing how these areas can be hard to be imaged and interpreted. a) Real seismic data showing a normal fault with apparent drag folding and an area with possible fault lenses. b) Geometric model and synthetic seismic, with a tem times upscaled model, 30 Hz dominant frequency and 45 deg angle illumination, from the Bartlett Wash, showing the difficulty of properly imaging fault lenses.

This same behaviour in relation to the resolution of these faults can be seen in Figure 7.7, where it is possible to observe that the closer the faults are, both in the real and synthetic seismic, the harder it becomes to correctly identify the reflectors contained in that area. The same figure also shows and example of normal fault behaviour along strike, or more specifically, the behaviour between two parallel normal faults that approach each other until they connect and merge with one another. As the areas chosen from the North Sea and the Moab Fault splay represent normal faults, it is not surprising that the seismic images produced from both areas produced similar results that can be used as analogues for one another.
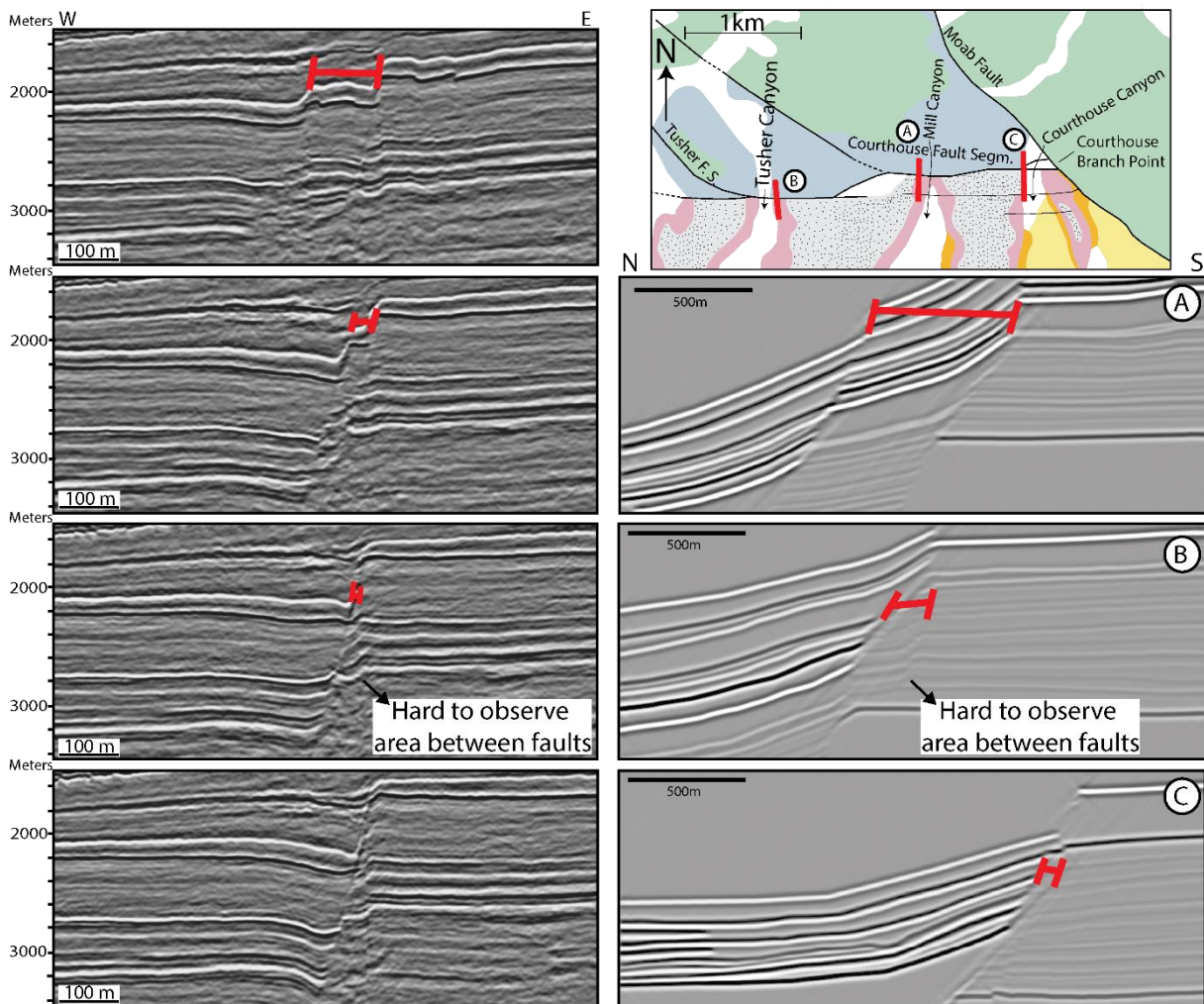
Figure 7.7: The evolution of a set of faults as the image is moved along strike. At one point, when both faults are close enough, the structures between the faults start to suffer from a loss of resolution. Although image B is located further into the fault splay in the synthetic seismic, it still holds a position in the faults splay for it to still serve as an analogue.

8. Conclusion and future work

8.1 Conclusion

This thesis aims to understand faults and fault zone complexities and how these complexities are imaged in seismic images. This was done by generating seismic images based on outcrops from the Moab Fault Splay and then further comparing these images with real seismic from the North Sea. From this process, the following conclusions were obtained:

- The internal structure of fault zones can change rapidly, in the study area at the kilometer scale. Such changes include variation in drag, fault splays, fault lenses and fault zone width, and may or may not be captured by seismic data.

- Using outcrops to produce geometric models is a reliable way to generate and obtain complex models that fit the real world. Their complexities are limited by the level of resolution available from field observation.

- The imaging of the faults and fault zones depends mainly on the displacement, dip and interaction of the surrounding stratigraphy.

- The results from the sensitivity analysis show that both seismic signature and detectability of faults and faults zones can be impacted by changes in dominant frequency, illumination angle, incident angle and noise level. The analysis in this work demonstrates how difficult it is to quantify a limit for detection, as it depends on multiple factors. The following conclusions can be drawn from the analysis:

  1 An increase in dominant frequency causes an increase in detectability.

  2 The illumination angle can deeply affect the image depending on the fault system being imaged. In this thesis, where a normal fault system with fault dips higher than 60° is used, only unrealistic high angles of illumination properly image the faults.

  3 The increase in incident angle will also cause a loss in detectability. However, depending on the curve behavior on the incident angle vs reflection coefficient graph from some of the units boundaries, they may have their reflection coefficient reduced to zero momentarily, which may reduce the visibility of faults, as it is also partially dependent on the visibility of the surrounding stratigraphy.

  4 The addition of noise deeply decreases the visibility of all structures present in the image, particularly smaller faults and fault tip zones. This reduction in

visibility happened as soon as just 25% of noise was added to the image in relation to the low amplitude reflectors.

- In extensional settings with high-angle normal faults, the parameters that could really impact the imaging would be the dominant frequency, as higher values allow for imaging of smaller displacement faults. Illumination could be another important parameter; however, as most faults in this scenario have dip-angles that frequently go above 60°, illumination angles above that mark become increasingly unrealistic to be obtained in real seismic.

- Possessing similar fault styles, the comparison between synthetic and real seismic images shows similar fault structures. With the knowledge of the seismic signatures produced by these fault complexities under seismic images, it is possible to infer that many of these signatures would also be present in the real seismic images

- Faults with a discrete offset not only are a challenge to be properly imaged, but may generate seismic reflectors that resemble fault drag. This is caused by reflector(s) appearing to be continuous and the problem will persist until the level of resolution where the actual discrete offset can be imaged.

- As faults represent a critical structure for fluid flow or mineralization, this study will help interpreters to assess faults and faults zones in a more realistic and critical way,creating a better understanding of the factors that may affect its visibility or be aware of possible pitfalls that may come in the form of sub seismic fault structures.

8.2 Suggestions for future work

- A 3D model based in the thesis study area could be generated to explore how the seismic response would differ when adding the third dimension. The gaps in fault geometry could, for example, be filled with the help of the RapidGeology software, and the result could be imported to SeixRoX.

- As the elastic parameters used in this thesis were based on dry wells, further investigations could use parameters from units saturated in oil or gas for comparison.

- Usage of different elastic parameters for faults zone, e.g., giving different parameters to the damage zone and fault core, to better understand the seismic response when this difference is applied

- Since most of the footwall modelled in this thesis was made up of eolian sandstones, other lithologies could have different fault zones structures that may impact seismic modelling.

9. References

Andersen, C. T. 2014. Seismic modelling of plaster models deformed in extension and contraction. Retrieved from https://bora.uib.no/bora-xmlui/handle/1956/9183

Bailey, W. R., Manzocchi, T., Walsh, J. J., Keogh, K., Hodgetts, D., Rippon, J. 2002. The effect of faults on the 3D connectivity of reservoir bodies: a case study from the East Pennine Coalfield, U.K. Pet. Geosciences 8, 263-277.

Barbeau, D. L. 2003. A flexural model for the Paradox Basin: implications for the tectonics of the Ancestral Rocky Mountains. Basin Research 15, 97-115.

Bauck, M. S., Faleide, J. I., Fossen, H. 2021. Late Jurassic to Late Cretaceous canyons on the Måløy Slope: Source to sink fingerprints on the northernmost North Sea rift margin, Norway. Norwegian Journal of geology 101, 1-30.

Berg, S. S., & Skar, T. 2005. Controls on damage zone asymmetry of a normal fault zone: outcrop analyses of a segment of the Moab fault, SE Utah. Journal of Structural Geology 27, 1803- 1822.

Braathen, A., Tveranger, J., Fossen, H., Skar, T., Cardozo, N., Semshaug, S.E., Bastesen, E., Sverdrup, E. 2009. Fault facies and its application to sandstone reservoirs. American Association of Petroleum Geologists Bulletin 93, 891-917.

Bradaric, A. D., Andersen, T., Lecomte, I., Løseth, H., Eide, C. H. 2021. Recognition and charaterization of small-scale sand injectites in seismic data: implications for reservoir development. Journal of the Geological Society 179(6).

Caine, J. S., Evans, J. P., Forster, C. B. 1996. Fault zone architecture and permeability structure. Geology 24, 1025-1028.

Carcione, J. M., Herman, G. C., & Kroode, A. P. E. t. 2002. Seismic modeling. Geophysics, 67(4), 1304-1325. doi:10.1190/1.1500393

Cartwright, J. A., Trudgill, B. D., Mansfield, C. S. 1995. Fault growth by segment linkage: an explanation for scatter in maximum displacement and trace length data from the Canyonlands Grabens of SE Utah. Journal of Structural Geology 17 (9), 1319-1326.

Childs, C., Watterson, J., Walsh, J.J. 1996. A model for the structure and development of fault zones. Geol. Soc. Lond. 153, 337-340.

Choi, J. H., Edwards, P., Ko, K., Kim, Y. S. 2016. Definition and classification of fault damages zones: A review and a new methodological approach. Earth-Sciences Reviews 152, 70-87.

Davatzes, N. C., Aydin, A., Eichhubl, P. 2003. Overprinting faulting mechanisms during the development of multiple fault sets in sandstone, Chimney Rock fault array, Utah, USA. Tectonophysics. 363, 1-18.

Davatzes, N. C., Aydin, A. 2005. Distribution and nature of fault architecture in a layered sandstone and shale sequence: An example from the Moab fault, Utah, AAPG Memoir 85, p. 153 –180.

Davatzes, N. C., Eichhubl, P., Aydin, A. 2005. Structural evolution of fault zones in sandstone by multiple deformation mechanisms: Moab fault, Southeast Utah. Geological Soc. Am. Bull., 117, 135-148.

Dimmen, V., Rotevatn, A., Lecomte, I. 2023. Imaging of small-scale faults in seismic reflection data: Insights from seismic modelling of faults in outcrop. Marine and Petroleum Geology 147, 1-16.

Doelling, H. H. 1988. Geology of the Salt Valley anticline and the Arches National Park, Grand County, Utah. In: Salt Deformation in the Paradox Region. Utah Geol. Survey Bull, 122, 7-58.

Doeling, H. H. 2002. Geologic map of the Moab and eastern part of the San Rafael Desert 30' x 60' Quadrangles, Grand and Emery Counties, Utah and Mesa County, Colorado. Utah Geological Survey Map 180.

Eide, C. H., Schofield, N., Lecomte, I., Buckley, S. J., and Howell, J. A. (2018). Seismic interpretation of sill complexes in sedimentary basins: implications for the sub-sill imaging problem. Journal of the Geological Society, 175(2):193–209.

Faleide, T. S., Braathen, A., Lecomte, I., Mulrooney, M. J., Midtkandal, I., Bugge, A. J., Planke, S. 2021. Impacts of seismic resolution on fault interpretation: Insights from seismc modelling. Tectonophysics 816, 1-19.

Faleide, T. S., Braathen, A., Lecomte, I. Anell. I. 2022. Exploring seismic detection and resolution thresholds of fault zones and gas seeps in the shallow subsurface using seismic modelling. Marine and Petroleum Geology 143, 1-18.

Flæte, C. P. 2022. Seismic imaging of faults and fault zones: insight through modelling for improved interpretation. Retrieved from https://bora.uib.no/bora-xmlui/handle/11250/2999392

Fossen, H. (2020). Chapter 8 - Fault classification, fault growth and displacement. In N. Scarselli, J. Adam, D. Chiarella, D. G. Roberts, & A. W. Bally (Eds.), Regional Geology and Tectonics (Second Edition) (pp. 119-147): Elsevier.

Fossen, H., Johansen, T. E. S., Hesthammer, J., & Rotevatn, A. 2005. Fault interaction in porous sandstone and implications for reservoir management; examples from southern Utah. AAPG Bulletin 89, 1593-1606.

Fossen, H., & Rotevatn, A. 2016. Fault linkage and relay structures in extensional settings—A review. Earth-Science Reviews 154, 14-28.

Foxford, K. A., Garde, I. R., Guscott, S. C. Burley, S. D., Lewis, J. J. M., Walsh, J. J. Watterson, J. 1996. The field geology of the Moab Fault. In: Geology and Resources of the Paradox Basin. Utah Geological Association Guidebook, 265-283

van Gent, H., Urai, J. L. 2020. Abutting faults: a case study of evolution of strain at Courthouse branch point, Moab Fault, Utah. Solid Earth 11, 513-526.

Grasemann, B., Martel, S., Passchier, C. W. 2005. Reverse and normal drag along fault.Journal of Structural Geology 27, 999-1010.

Gudmundsson, A., Simmenes, T. H., Larsen, B., Philipp, S. L. 2010. Effects of internal structure and local stresses on fracture propagation, deflection and arrest in fault zones. Journal of Structural Geology 32, 1643-1655.

Hamblin, W. K. 1965. Origin of 'reverse drag' on the down-thrown side of normal faults. Geological Society of America Bulletin 76, 1145–1164.

Jackson, C., Osagiede, E., Duffy, O., & Wrona, T. 2014. Quantifying the growth history of seismically-imaged normal faults: the impact of vertical seismic resolution. Journal of structural geology.

Jensen, K., Lecomte, I., Gelius, L. J., & Kaschwich, T. 2021. Point-spread function convolution to simulate prestack depth migrated images: A validation study. Geophysical Prospecting, 69(8-9), 1571-1590.

Johansen, T. E. S., Fossen, H., Kluge, R. 2005. The impact of syn-faulting porosity reduction on damage zone architecture in porous sandstone: Na outcrop example from the Moab Fault, Utah. Journal of Structural Geology. 27. 1469-1485.

Johansen, T. E. S., Fossen, H. 2008. Internal geometry of fault damage zones in interbedded siliciclastic sediments. Geological Society, Special Publications. 299. 35-56.

Kearey, P. 1993. The Encyclopedia of the Solid Earth Sciences. Blackwell Science, Oxford.

Kim, Y. S., Peacock, D. C. P., Sandersom, D. 2004. Fault damage zones. Journal of Structural Geology 26, 503-517.

Knott, S. D., Beach, A., Brockbank, P. J., Brown, J. L., McCallum, J. E., & Welbon, A. I. 1996. Spatial and mechanical controls on normal fault populations. Journal of Structural Geology 18, 359-372.

Lecomte, I. 2008. Resolution and Illumination analyses in PSDM: A ray-based approach. Geophysics, 27.

Lecomte, I., Lubrano-Lavadera, P., Anell, I., Buckley, S., Schmid, D. W., and Heeremans, M. 2015. Ray-based seismic modeling of geologic models: Understanding and analyzing seismic images efficiently. Interpretation 3, 71-89.

Lecomte, I., Lubrano-Lavadera, P., Botter, C., Anell, I., Buckley, S., Eide, C., Grippa, A., Mascolo, V., Kjoberg, S. 2016. 2(3)D convolution modelling of complex geological targets – beyond 1D convolution. First Break, 34, 99-107.

Lindanger, M., Gabrielsen, R. H., & Braathen, A. 2007. Analysis of rock lenses in extensional faults. Norwegian Journal of Geology/Norsk Geologisk Forening, 87(4). Lindanger, R., Øygaren, M., Gabrielsen, R., Mjelde, R., Randen, T., & Tjøstheim, B. (2004). Analogue (plaster) modelling and synthetic seismic representation of hangingwall fault. first break, 22(1)

Loveless, S., Bense, V., Turner, J. 2011. Fault architecture and deformation processes within poorly lithified rift sediments, Central Greece. Journal of Structural Geology 33, 1554-1568.

Maerten, L., Gillespie, P., Pollard, D. D. 2002. Effects of local stress perturbation on secondary fault development. Journal of Structural Geology 24, 145-153.

Nixon, C. W., Sanderson, D. J., Dee, S. J., Bull, J. M., Humphreys, R. J., & Swanson, M. H. 2014. Fault interactions and reactivation within a normal-fault network at Milne Point, Alaska. AAPG Bulletin 98, 2081-2107.

Peacock, D. 1991. Displacement and segment linkage in strike-slip fault zones. Journal of Structure Geology 13, 1025-1035.

Peacock, D., Sanderson, D. 1991. Displacement, segment linkage and relay ramps in normal fault zones. Journal of Structural Geology 13, 721-733.

Peacock, D., Sanderson, D. 1994. Geometry and development of relay ramps in normal fault systems. AAPG Bulletin 78, 147-165.

Peacock, D., Nixon, C. W., Rotevatn, A. Sanderson, D. J., Zuluaga, L. F. 2016. Glossary of fault and other fracture networks.

Peacock, D., Nixon, C. W., Rotevatn, A., Sanderson, D. J., Zuluaga, L. F. 2017. Interacting faults. Journal of Structural Geology 97, 1-22.

Rabbel, O., Galland, O., Mair, K., Lecomte, I., Senger, K., Spacapan, J. B., Manceda, R. 2018. From field analogues to realistic seismic modelling: a case study of an oil-producing andesitic sill complex in the Neuquén Basin, Argentina. Journal of Geological Society 175 (4).

Rotevatn, A., Fossen, H. 2011. Simulating the effect of subseismic fault tails and process zones in a siliciclastic reservoir analogue: Implications for aquifer support and trap definition. Marine and petroleum geology 28, 1648-1662.

Rotevatn, A., Fossen, H., Hesthammer, J., Aas, T. E., & Howell, J. A. 2007. Are relay ramps conduits for fluid flow? Structural analysis of a relay ramp in Arches National Park, Utah. Geological Society, London, Special Publications 270, 55-71.

Sanderson, D. J., Zhang, X. 1999. Critical stress localization of flow associated with deformation of well-fractured rock masses, with implications for mineral deposits. Geological Society, London, Special Publications 155, 69-81.

Schueller, S., Braathen, A., Fossen, H., Tveranger, J. 2013. Spatial distribution of deformation bands in damage zones of extensional faults in porous sandstones: Statistical analysis of field data. Journal of Structural Geology 52, 148-162.

Shipton, Z., Cowie, P. 2001. Damage zone and slip-surface evolution over μm to km scales in high-porosity Navajo sandstone, Utah. Journal of Structural Geology 23, 1825-1844.

Simm, R., Bacon, M. 2014. Seismic wavelets and resolution, page 23–37. Cambridge: Cambridge University Press.

Soliva, R., Benedicto, A., Maerten, L. 2006. Spacing and linkage of confined normal faults: importance of mechanical thickness. Journal of Geophys. Res. Solid Earth 111.

Stockton, S. L., Balch, A. H. 1978. The utility of pretoleum seismic exploration data in delineating structural features within salt structures. United States Departament of the Interior Geological Survey.

Trudgill, B. D. 2011. Evolution of salt structures in the northern Paradox Basin: controls on evaporite deposition, salt wall growth and supra-salt stratigraphic architecture. Basin Research 23, 208-238.

Volatili, T., Agosta, F., Cardozo, N., Zambrano, M., Lecomte, I., Tondi, E. 2022. Outcrop-scale fracture analysis and seismic modelling of a basin-bounding normal fault in plataform carbonates, central Italy. Journal of Structural Geology 155, 1-18.

Walsh, J. J., Nicol, A., Childs, C. 2002. Na alternative model for the growth of faults. Journal of Structural Geology 24, 1669-1675.

Walsh, J. J., Bailey, W. R., Childs, C., Nicol, A., Bonson, C. G. 2003. Formation of segmented normal faults: a 3-D perspective.

Zhang, X., Sanderson, D. J. 1996. Effects of stress on the two-dimensional permeability tensor of natural fracture networks. Geophysical Journal International 125, 912-924.

Appendices

Appendix A

Seismic modelling results

The link below will lead to a Powerpoint presentation containing all results from the seismic modelling from the outcrops in Utah.

Link: [Seismic modelling results Thesis Lucas.pptx (figshare.com)](figshare.com)

Appendix B

Mat-Lab Script

```matlab
fname          = 'PNGpanel_BW32bits';   % figure name (NB! grey codes,
32-bit!)
x_max          = 1504;      % number of pixels as columns (horizontal
axis)
mpvp           = 1;          % no need to change; not used.
% Add path to SeisLab
addpath('SeisLab 3.02/S4M/Geophysics_3.0');
% Setup SeisLab presets
presets;
global S4M;
% Read image
[A,map]              = imread([fname, '.png']);
imshow(A,map);
colorbar;
A = squeeze(A(:,:,1))
%% DATA decomposition
[n m] = size(A);
block = zeros(n,m);
vp = zeros(n,m); % NB! in km/s  (NORSAR default unit)
vs = zeros(n,m); % NB! in km/s  (NORSAR default unit)
rho = zeros(n,m); % NB! in kg/dm3 or equiv. (NORSAR default unit)
noise = zeros(n,m); % white noise
for i = 1:n
    for j = 1:m
        if A(i,j) == 225 % facies 1
            block(i,j) = 1. ;
            vp(i,j) = 3.7 ;
        elseif A(i,j) == 76 % facies 2
            block(i,j) = 2. ;
            vp(i,j) = 4.0 ;
        elseif A(i,j) == 104 % facies 3
            block(i,j) = 3.0 ;
            vp(i,j) = 3.5 ;
        elseif A(i,j) == 180 % facies 4
            block(i,j) = 4. ;
            vp(i,j) = 3.6 ;
         else
          block(i,j) = 5. ; % NB! in case of holes in model! water
Vp
            vp(i,j) = 1.5 ;
        end
        vs(i,j) = vp(i,j) / 2.; % constant Vp/Vs ratio
        rho(i,j) = 0.31*((vp(i,j)*1000.)^0.25); % original Gardner
relation
    end
```

```matlab
% create white noise grid with same size (number of pixels
vertically)
        cn = dsp.ColoredNoise('Color','white','SamplesPerFrame',m);
%% colored noise function
        x = cn();
        noise(i,:) = x /20.; %(NB! average noise 1, but reduced by
20. here)
        clear('cn','x')
end
% Trace of seismic line
X           = linspace(0, x_max, size(A,2));
Y           = zeros(size(X));
% Create data structure - block
seis_fold.type              = 'seismic';
seis_fold.tag               = 'unspecified';
seis_fold.name              = fname;
seis_fold.line_number       = 1;
seis_fold.reel_number       = 1;
seis_fold.traces_per_record = size(A,2);
seis_fold.aux_per_record    = size(A,2);
seis_fold.cdp_fold          = 1;
seis_fold.first             = 0;
seis_fold.last              = size(A,1)-1;
seis_fold.step              = mpvp;
seis_fold.units             = 'm';
seis_fold.traces            = block;
seis_fold.null              = [];
seis_fold.header_info       = {...
    'sou_x'         'm'      'X coordinate of source'
    'sou_y'         'm'      'Y coordinate of source'
    'rec_x'         'm'      'X coordinate of receiver'
    'rec_y'         'm'      'Y coordinate of receiver'};
seis_fold.headers           = [X; Y; X; Y];
seis_fold.fp_format_of_segy_file    = 'ibm';
% Write segy
write_segy_file(seis_fold, [fname, '_block.sgy']);
% Read
seis_read = read_segy_file( [fname, '_block.sgy']);
% Plot
s_cplot(seis_read, {'colormap','jet'},{'title','Block
#'},{'time_lines',}, {'limits', min(block(:)), max(block(:))});
c = colorbar;
c.Label.String = '#';
% Create data structure - vp
seis_fold.type              = 'seismic';
seis_fold.tag               = 'unspecified';
seis_fold.name              = fname;
seis_fold.line_number       = 1;
seis_fold.reel_number       = 1;
seis_fold.traces_per_record = size(A,2);
seis_fold.aux_per_record    = size(A,2);
seis_fold.cdp_fold          = 1;
seis_fold.first             = 0;
seis_fold.last              = size(A,1)-1;
seis_fold.step              = mpvp;
seis_fold.units             = 'm';
```

```matlab
seis_fold.traces            = vp;
seis_fold.null              = [];
seis_fold.header_info       = {...
    'sou_x'         'm'         'X coordinate of source'
    'sou_y'         'm'         'Y coordinate of source'
    'rec_x'         'm'         'X coordinate of receiver'
    'rec_y'         'm'         'Y coordinate of receiver'};
seis_fold.headers           = [X; Y; X; Y];
seis_fold.fp_format_of_segy_file    = 'ibm';
% Write segy
write_segy_file(seis_fold, [fname, '_vp.sgy']);
% Read
seis_read = read_segy_file( [fname, '_vp.sgy']);
% Plot
s_cplot(seis_read, {'colormap','jet'},{'title','Vp
(km/s)'},{'time_lines',}, {'limits', min(vp(:)), max(vp(:))});
c = colorbar;
c.Label.String = 'Vp (km/s)';
% Create data structure - vs
seis_fold.type              = 'seismic';
seis_fold.tag               = 'unspecified';
seis_fold.name              = fname;
seis_fold.line_number       = 1;
seis_fold.reel_number       = 1;
seis_fold.traces_per_record = size(A,2);
seis_fold.aux_per_record    = size(A,2);
seis_fold.cdp_fold          = 1;
seis_fold.first             = 0;
seis_fold.last              = size(A,1)-1;
seis_fold.step              = mpvp;
seis_fold.units             = 'm';
seis_fold.traces            = vs;
seis_fold.null              = [];
seis_fold.header_info       = {...
    'sou_x'         'm'         'X coordinate of source'
    'sou_y'         'm'         'Y coordinate of source'
    'rec_x'         'm'         'X coordinate of receiver'
    'rec_y'         'm'         'Y coordinate of receiver'};
seis_fold.headers           = [X; Y; X; Y];
seis_fold.fp_format_of_segy_file    = 'ibm';
% Write segy
write_segy_file(seis_fold, [fname, '_vs.sgy']);
% Read
seis_read = read_segy_file( [fname, '_vs.sgy']);
% Plot
s_cplot(seis_read, {'colormap','jet'},{'title','Vs
(km/s)'},{'time_lines',}, {'limits', min(vs(:)), max(vs(:))});
c = colorbar;
c.Label.String = 'Vs (km/s)';
% Create data structure - rho
seis_fold.type              = 'seismic';
seis_fold.tag               = 'unspecified';
seis_fold.name              = fname;
seis_fold.line_number       = 1;
seis_fold.reel_number       = 1;
seis_fold.traces_per_record = size(A,2);
```

```matlab
seis_fold.aux_per_record    = size(A,2);
seis_fold.cdp_fold          = 1;
seis_fold.first             = 0;
seis_fold.last              = size(A,1)-1;
seis_fold.step              = mpvp;
seis_fold.units             = 'm';
seis_fold.traces            = rho;
seis_fold.null              = [];
seis_fold.header_info       = {...
    'sou_x'         'm'      'X coordinate of source'
    'sou_y'         'm'      'Y coordinate of source'
    'rec_x'         'm'      'X coordinate of receiver'
    'rec_y'         'm'      'Y coordinate of receiver'};
seis_fold.headers           = [X; Y; X; Y];
seis_fold.fp_format_of_segy_file    = 'ibm';
% Write segy
write_segy_file(seis_fold, [fname, '_rho.sgy']);
% Read
seis_read = read_segy_file( [fname, '_rho.sgy']);
% Plot
s_cplot(seis_read, {'colormap','jet'},{'title','Density
(kg/dm3)'},{'time_lines',}, {'limits', min(rho(:)), max(rho(:))});
c = colorbar;
c.Label.String = 'Rho (kg/dm3)';
% Create data structure - noise
seis_fold.type              = 'seismic';
seis_fold.tag               = 'unspecified';
seis_fold.name              = fname;
seis_fold.line_number       = 1;
seis_fold.reel_number       = 1;
seis_fold.traces_per_record = size(A,2);
seis_fold.aux_per_record    = size(A,2);
seis_fold.cdp_fold          = 1;
seis_fold.first             = 0;
seis_fold.last              = size(A,1)-1;
seis_fold.step              = mpvp;
seis_fold.units             = 'm';
seis_fold.traces            = noise;
seis_fold.null              = [];
seis_fold.header_info       = {...
    'sou_x'         'm'      'X coordinate of source'
    'sou_y'         'm'      'Y coordinate of source'
    'rec_x'         'm'      'X coordinate of receiver'
    'rec_y'         'm'      'Y coordinate of receiver'};
seis_fold.headers           = [X; Y; X; Y];
seis_fold.fp_format_of_segy_file    = 'ibm';
% Write segy
write_segy_file(seis_fold, [fname, '_noise.sgy']);
% Read
seis_read = read_segy_file( [fname, '_noise.sgy']);
% Plot
s_cplot(seis_read, {'colormap','jet'},{'title','White
noise'},{'time_lines',}, {'limits', min(noise(:)), max(noise(:))});
c = colorbar;
c.Label.String = 'Noise value';
```